Habtamu W. Tesfaw[1], Habtamu W Tesfaw[2], Ilkka I Virtanen[2], and Anita T Aikio[2]

[1]Affiliation not available
[2]Space Physics and Astronomy Research Unit, University of Oulu

May 25, 2023

Abstract

Key Points:

* We use EISCAT UHF ISR data to study the 1-100 keV electron precipitation at 6 66.7° MLAT observed during 21 years.

* The auroral electron precipitation occurrence rate as observed by the radar reaches70% in the 05–06 MLT sector of the main auroral oval.

* Electron precipitation with 50–100 keV peak energies is more common than with 30–50 keV peak energies after 06 MLT

Characteristics of auroral electron precipitation at geomagnetic latitude 67° over Tromsø

Habtamu W. Tesfaw[1], Ilkka I. Virtanen[1], Anita T. Aikio[1]

[1]Space Physics and Astronomy Research Unit, University of Oulu, Oulu, Finland

Key Points:

- We use EISCAT UHF ISR data to study the 1–100 keV electron precipitation at 66.7° MLAT observed during 21 years
- Large auroral powers ($\geq$60 mWm^{-2}) are observed in the 18–02 MLT sector, and mainly in the main auroral oval
- Peak energies higher than 50 keV are observed only after 22 MLT and preferentially in the 06–11 MLT sector of the diffuse auroral oval

Corresponding author: Habtamu W. Tesfaw, `habtamu.tesfaw@oulu.fi`

Abstract

We use the EISCAT incoherent scatter radar data measured in years 2001–2021 to study statistical characteristics of 1–100 keV electron precipitation at 66.7° MLAT over Tromsø. Peak energies, auroral powers and number fluxes of precipitating electrons are derived from electron density altitude profiles measured along the geomagnetic field line during periods of no photoionization. The method allows us to include energetic 30–100 keV electrons, which are poorly covered in earlier satellite-based studies. Locations of the radar within the auroral oval are determined using a model with the 1-h Hpo geomagnetic index as input. We find that occurrence rate of electron precipitation in Tromsø peaks during the declining phases of solar cycles (sc), in 2002–2004 for sc23 and in 2015–2017 for sc24. The occurrence rate variations match with Hpo > 2, indicating that they are caused by variations in geomagnetic activity. The occurrence rate has maxima during March and September and minimum in December to January. In addition, the occurrence frequency increases continuously from evening to morning hours, reaching maximum at 05–06 MLT. This MLT variation is caused mainly by the motion of the radar site with respect to the auroral oval as the Earth rotates under the oval. The peak energy distribution is dominated by 1–5 keV energies from dusk until dawn, and by 5–10 keV energies at 06–09 MLT. Peak energies higher than 50 keV are observed only after 22 MLT and preferentially in the 06–11 MLT sector of the diffuse auroral oval. Large auroral powers (> 60 mWm^{-2}) are observed in the 18–02 MLT sector in the main auroral oval.

Plain Language Summary

The Earth's magnetic field is almost vertical at high latitudes, and it connects the upper part of the Earth's atmosphere to the surrounding magnetosphere. This connection allows electrons to precipitate from the magnetosphere down to the upper atmosphere, and causes the visual auroral displays, geomagnetic disturbances, and ionization of the neutral atmospheric particles through collisions. We use more than 20 years of radar data measured by the EISCAT incoherent scatter radar in Tromsø, northern Norway, to study statistical characteristics of auroral electron precipitation. The radar data allows us to include not only 1–30 keV but also 30–100 keV energies, which have been poorly covered in previous satellite-based studies. We find that the radar observes auroral electron precipitation most frequently during morning hours (5–6 magnetic local time), and during September and March equinox months. In addition, electron precipitation occurs most frequently during years immediately after the sunspot maximum years. Electrons that have higher energies precipitate more commonly during morning hours than evening hours, and large energy and number fluxes occur more frequently in the evening and pre-midnight hours than in post-midnight and morning hours.

1 Introduction

Electron precipitation is one of the major energy input mechanisms to the high latitude upper atmosphere. The energy is deposited in the auroral ionosphere, where the precipitation causes auroral emissions, ionizes the neutral atmosphere, enhances ionospheric conductivity, alters neutral and ion compositions, and heats the ambient electron gas (Palmroth et al., 2021). Auroral electron precipitation is characterized by the global distribution of the auroral power (total energy flux), total number flux and peak energy of the precipitating electrons (Virtanen et al., 2018; Kaeppler et al., 2020; Tesfaw et al., 2022).

Several statistical studies have characterized the global distribution of electron precipitation using satellite measurements. Hardy et al. (1985) used the SSJ/3 instruments onboard the DMSP satellites that detect fluxes of 50 eV–20 keV auroral electrons. The authors studied statistical variations in the average energy, total energy flux and total

number flux of electron precipitation as function of magnetic local time (MLT), magnetic latitude, and the geomagnetic Kp index. Newell et al. (2009, 2010) used the upgraded SSJ/4 instrument onboard the same satellite series to study statistical features of discrete and diffuse auroral electron precipitation at 30 eV–30 keV energies. The authors investigated MLT, seasonal, and solar activity variations of the energy and number fluxes. Vorobjev et al. (2013) used the same instrument to develop an interactive auroral oval model, which shows MLT and magnetic activity variation of the average energy and energy flux of precipitating electrons. Hardy et al. (1991) combined measurements from the SSJ/3 and SSJ/4 instruments to characterize global distribution of average energy, auroral power, number flux, and the derived ionospheric conductivity. A shortcoming of the DMSP measurements is that the highest electron energy covered by the SSJ instruments is 30 keV.

High energy (> 30 keV) electrons have been studied using the MEPED instrument (Evans & Greer, 2004) onboard the POES satellites (Wissing et al., 2008; Lam et al., 2010; Yakovchuk & Wissing, 2019). Focus of these studies was on MLT and magnetic activity variations of electron number fluxes. The MEPED instruments have only three wide energy bands (30–100 keV, 100–300 keV and 300–2500 keV), which makes calculation of peak energy and auroral power estimates impractical.

Newell et al. (2001) used the Global Ultraviolet Imager (GUVI) onboard the Polar satellite to study variations of auroral power with substorm phases within different MLT sectors. The GUIVI instrument onboard TIMED satellite was used by Zhang and Paxton (2008) to develop a Kp index dependent empirical model that shows global distribution of the average energy and auroral power. The same instrument was used by Liou et al. (2001), who studied seasonal variation of auroral power. The GUVI studies combine the short and long Lyman-Birge-Hopfield (LBHS and LBHL) N_2 auroral emissions in the FUV spectrum with auroral and airglow models to estimate the average energy and energy flux of the precipitating electrons.

The satellite studies show that electron precipitation is typically more energetic in the morning side than in the evening side of the auroral oval (Hardy et al., 1985, 1991; Wissing et al., 2008; Lam et al., 2010). Larger auroral powers are measured during active geomagnetic conditions than during low geomagnetic activity (Hardy et al., 1985, 1991; Zhang & Paxton, 2008; Vorobjev et al., 2013; Yakovchuk & Wissing, 2019), and the MLT sector of highest energy flux moves from pre-midnight to post-midnight with increasing geomagnetic activity (Hardy et al., 1985). Newell et al. (2009) found that most of the energy carried by discrete and diffuse auroral electrons dissipate in the pre-midnight and post-midnight side of the auroral oval, respectively.

Incoherent scatter radar (ISR) measurements of geomagnetic field-aligned electron density profiles can be inverted into differential energy fluxes of the precipitating electrons. Several different techniques have been developed for the energy spectra inversion (Vondrak & Baron, 1977; Kirkwood, 1988; Brekke et al., 1989; Dahlgren et al., 2011; Semeter & Kamalabadi, 2005; Kaeppler et al., 2015; Simon Wedlund et al., 2013; Virtanen et al., 2018). In this study, we derive the auroral power, peak energy, and number flux of precipitating electrons from the EISCAT Tromsø UHF incoherent scatter radar measurements conducted between 2001 and 2021. We use the ELectron SPECtrum (ELSPEC) method (Virtanen et al., 2018) that yields estimates for 1–100 keV auroral electrons. We carry out a statistical study of local electron precipitation characteristics, including 30–100 keV electrons that are poorly covered by satellite measurements. In order to put the local measurements into a more global context, we use an empirical Kp dependent model of the auroral oval location (Starkov, 1994). To our knowledge, this is the first study that uses ISR measurements for a long-term statistical study of electron precipitation characteristics.

The paper is organized as follows. In Section 2 we describe the data selection and data analysis. Statistical results of peak energy, auroral power, and total number flux of electron precipitation are shown in Section 3. Discussion on effects of the auroral oval motion on our results, seasonal and solar cycle variation of precipitation occurrence rate and comparison with earlier results are given in Section 4, and the final conclusions are in drawn Section 5.

2 Data analysis

2.1 Selection of EISCAT radar data

Our primary data are altitude profiles of electron density and electron temperature measured with the EISCAT Tromsø UHF incoherent scatter radar (69.58°N, 19.23°E geodetic; 66.67°N, 101.41°E geomagnetic) obtained from the Madrigal database. The data in Madrigal are analyzed using the Grand Unified Incoherent Scatter Design and Analysis Package (GUISDAP) (Lehtinen & Huuskonen, 1996). Altogether 10 days of data were re-analysed, because they appeared to be originally analysed with incorrect electron density calibration in GUISDAP. The data are a collection of numerous separate radar experiments conducted with different beam scanning patterns, transmission modulations and signal processing schemes. Different radar operation modes provide different resolutions, but the time resolution is typically close to 1 min, and the altitude resolution is a few kilometers in the E region. The radar data spans more than 20 years of radar observations conducted between January 2001 and April 2021.

Since electron precipitation occurs along the geomagnetic field lines, we select data from field-aligned measurements. These include the EISCAT CP1 mode with the radar beam fixed field-aligned, as well as field-aligned profiles from modes that contain several pointing directions. To exclude daytime measurements with photoionization, we exclude measurements during which the solar zenith angle (χ) at 100 km altitude was less than 90°.

Yearly, monthly and magnetic local time (MLT) distributions of the selected data are shown as yellow histograms in panels (a)–(c) of Figure 1. Panel (a) shows that number of data points per year varies approximately between 12000 and 34000. The number of measurements per year is not constant because the radar does not operate continuously and the observation modes vary. Exclusion of daylight measurements results in absence of data in the summer months of June, July and August (not shown here), and large reduction of data points between 10 and 14 MLT. Panel (b) shows that the data covers equinox and winter months from September to April, with a few additional measurements from May. MLT distribution in panel (c) shows that the number of data points peaks at MLT midnight and majority (more than 80 %) of the data are from the 18–06 MLT sector.

2.2 The ELSPEC method

ELSPEC (Virtanen et al., 2018) takes the field-aligned electron density and temperature profiles from 80 to 150 km altitudes as inputs, and calculates the differential number flux of 1–100 keV electron precipitation at selected energy bins. In this work, ELSPEC is set to solve the steady state electron continuity equation that involves the ion production and loss rates. The steady state assumption is justified by the long radar integration time (close to 1 min) which is longer than typical electron recombination time scales in the E region (Semeter & Kamalabadi, 2005). The ion production rates of mono-energetic electrons in the selected energy grid are calculated using the model of Fang et al. (2010). The model needs a neutral atmosphere, which is taken from the Mass Spectrometer Incoherent Scatter radar (MSIS) model (Picone et al., 2002). The ion loss rate is a product of an effective recombination coefficient and square of electron density. Re-
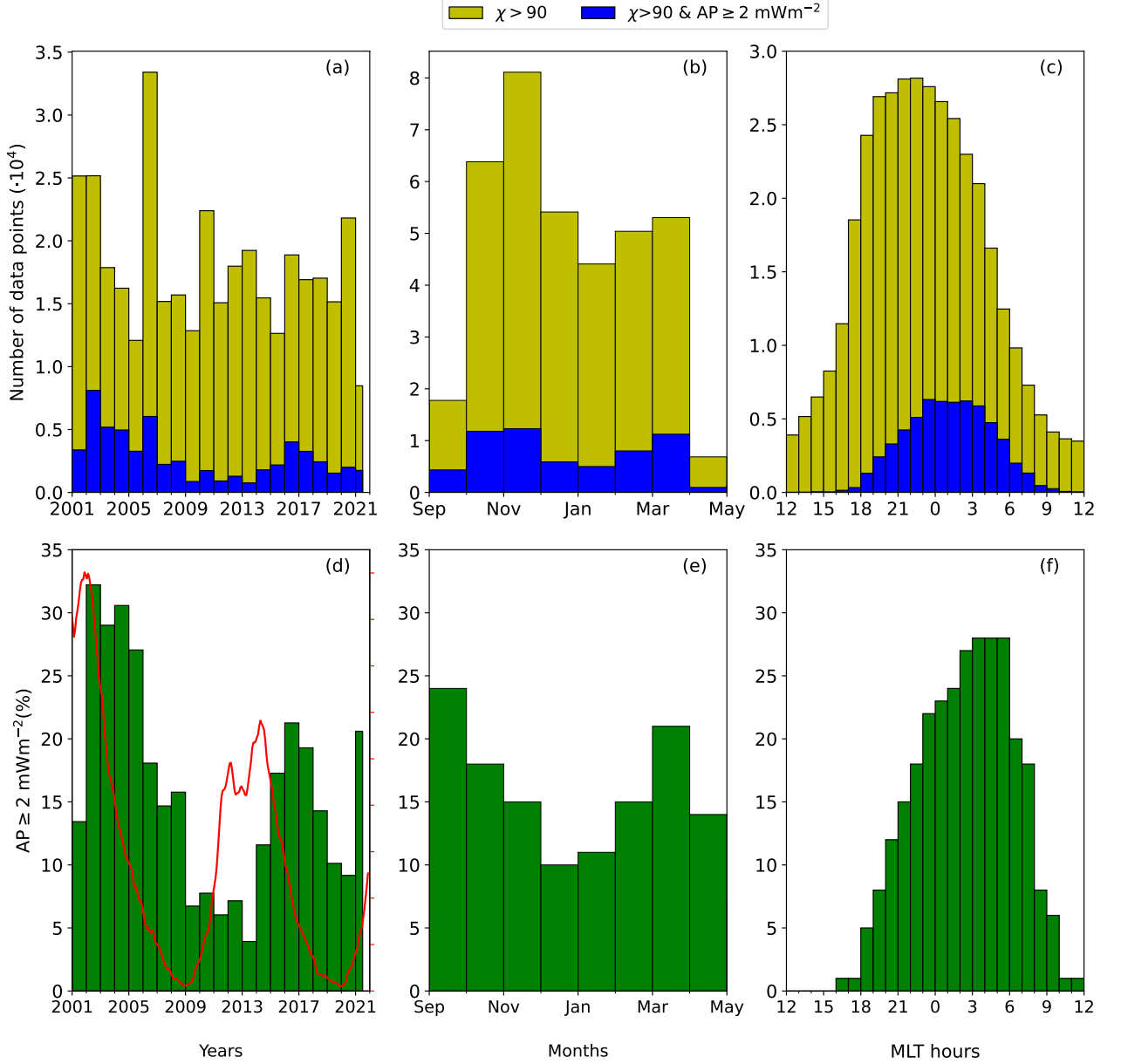
Figure 1. Yearly, monthly and MLT distribution of selected radar measurements. Top panels: all field-aligned measurements with solar zenith angle greater than 90° (yellow histograms), and data points with auroral power (AP) greater than 2 mWm^{-2} (blue histograms). Bottom panels: fraction of data points with auroral power larger than 2 mWm^{-2}. The sunspot number is shown by the red line in panel (d) and its maximum value is 180.

combination coefficients of NO$^+$ and O$_2^+$ ions are calculated using the results of Sheehan and St-Maurice (2004). The effective recombination coefficient depends also on electron temperature and ion composition, which are taken from the radar measurements and the International Reference Ionosphere (IRI) model (Bilitza et al., 2017), respectively.

ELSPEC iteratively minimizes the difference between the modelled and the measured electron density profiles to find a differential number flux that leads to best match with the measurements. The iteration is repeated with several different parametric spectrum models for each electron density profile, and the optimal model is selected using the Akaike information criterion (Burnham & Anderson, 2002, for example). The models can produce a variety of commonly observed electron energy spectra, for example Maxwellians, κ-distributions, and mono-energetic spectra, as well as more exotic spectrum shapes (Virtanen et al., 2018). Differential energy flux is calculated as product of the differential number flux and the corresponding electron energy in a given energy grid energy grid. Auroral power (total energy flux) and total number flux are integrated from the differential energy and number fluxes, correspondingly. Peak energy is the energy at which the differential energy flux reaches its maximum value.

As GUISDAP fits sometimes fail at individual altitudes, there are data points missing from the electron density and temperature profiles. The data gaps are filled by means of linear interpolation in middle of the profiles, or with IRI model data if data points are missing from either end of the profile. The selected values do not affect the ELSPEC fit results, because very large standard deviations (10^{12} m^{-3}) are given for the filled electron densities. An exception is the lowest measured altitude, where a small standard deviation (10^9 m^{-3}) is used to suppress unrealistic oscillations from the ELSPEC fits. This selection does not significantly affect the inverted spectra, because the IRI values used to fill missing data in the D region are small, and the GUISDAP fits tend to fail only when the true electron density is also small.

While ELSPEC is nominally using radar data from 80–150 altitudes, many experiment modes do not cover the lower ionosphere down to 80 km. As electron penetration depth increases with increasing energy, lack of measurements from the lowest altitudes allows the solver to produce almost any value for the flux at the highest energies. To remove those parts of the spectra that are not based on measurements, we use the lowest measured altitude h_{min} to select a maximum energy E_{max} for each measurement. Only energies up to E_{max} are used from each fitted energy spectrum when calculating peak energies, auroral powers, and total number fluxes. E_{max} is selected so that ion production by mono-energetic electrons with energy E_{max} peaks at h_{min}. For example, $E_{max} \approx$ 100 keV for $h_{min} = 80$ km, and $E_{max} \approx 45$ keV for $h_{min} = 90$ km.

The final ELSPEC fit results were manually inspected for unrealistic results. Based on this search, 20 out of 2000 separate Madrigal data files were rejected. Duration of Madrigal data file varies from a few hours to 24 h. In addition, individual fits with normalized sum of squared residuals (chi-squared) larger than 3 were rejected to remove outliers caused e.g. by space debris echoes.

2.3 Yearly, monthly and MLT distributions of electron precipitation

As described above, we use all field-aligned EISCAT Tromsø UHF radar data with solar zenith angle larger than 90° available in the Madrigal data base from 2001 to 2021. The data are analysed with ELSPEC into peak energies, auroral powers, and total number fluxe estimates. After the ELSPEC analysis, we divide the data into two groups according to the auroral power. Only data with auroral power larger than 2 mWm^{-2} are used for studies of peak energy, auroral power, and total number flux. The criterion selects the data points that show clear signs of electron precipitation and are accurate enough for reliable peak energy estimation. As the electron precipitation is the only source of ionization in the night-time E region, the ISR data are noisy when the auroral power is small.

Yearly, monthly and MLT distributions of the final ELSPEC results with auroral power larger than 2 mWm^{-2} are shown as blue histograms in panels a, b, and c of Figure 1. Rejecting data points with auroral power less than 2 mWm^{-2} reduces the num-
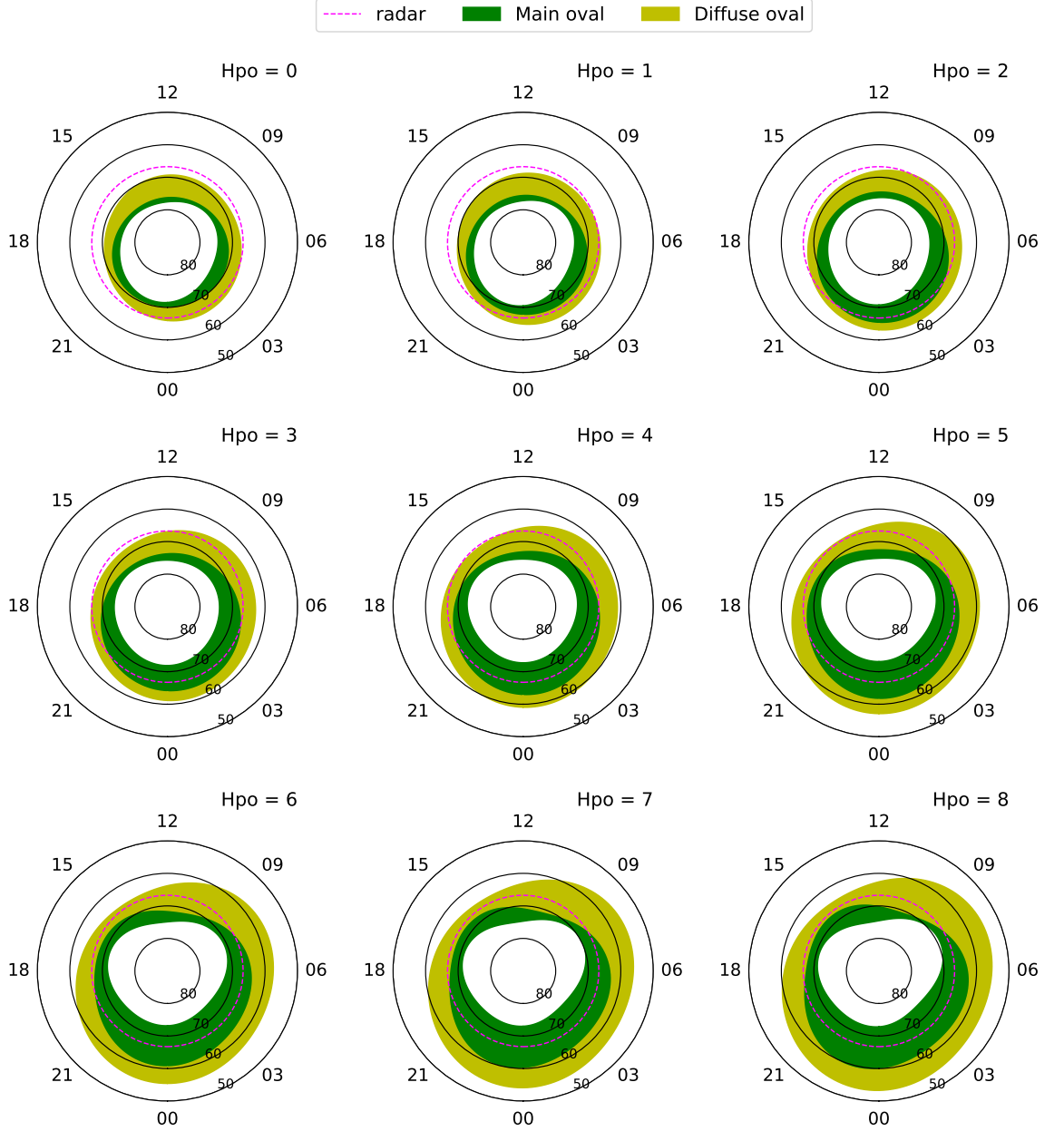
Figure 2. The main (green) and diffuse (yellow) Feldstein-Starkov auroral ovals as function of magnetic latitude and magnetic local time for different Hpo levels. The dotted line is location of the EISCAT Tromsø UHF incoherent scatter radar.

ber of data points per year by 65–95%, per month by 75–95%, and per MLT bin by 70–100%. The large differences are related to variations in precipitation occurrence rates in Tromsø and are discussed in more detail in Sections 3.1, 4.1 and 4.2.

2.4 Location of the radar relative to the auroral oval

Our data are measured at a fixed point on Earth that rotates under the auroral oval. The shape and size of the oval depend on geomagnetic activity. As a result, the

location of the radar beam with respect to the auroral oval varies, and the radar sometimes observes regions outside of the oval. Interpretation of our results thus requires taking into account the position of the radar beam with respect to the auroral oval for each data point. We determine the location of the auroral oval by using the Feldstein-Starkov auroral oval model (Starkov, 1994; Sigernes et al., 2011). The model gives the poleward and equatorward boundaries of the main and diffuse auroral ovals as a function of Kp index and MLT. As input to the model, we use the Hpo index (Yamazaki et al., 2022) which has better temporal resolution than the traditional 3-hour Kp index. The Hpo index has two versions with 30 and 60 min temporal resolutions, and for this study we use the 60 min version.

Figure 2 shows the main (green) and diffuse (yellow) auroral ovals as function of magnetic latitude and magnetic local time for Hpo = 0–8. The radar beam position is shown as a dotted circular line. The figure shows that the main oval is wider in the night side than in the day side. The diffuse oval is wider than the main oval for low Hpo values. Size of the oval and the day-night asymmetry increase with increasing Hpo index. When Hpo is higher than 6, the main and diffuse ovals extend to magnetic latitudes as low as 60°and 55°, respectively.

The MLT intervals during which the radar is within the main and diffuse ovals at different Hpo levels are shown in the last two columns of Table 1. Both the oval plots and the table indicate that the radar beam enters the oval earlier in the evening and leaves it later in the morning when the oval grows larger with increasing Hpo. When Hpo is below 2, the radar beam is always outside of the main oval, but reaches the diffuse oval during night and early morning hours. When Hpo is larger than 4, the radar beam is always poleward of the equatorward boundary of the diffuse oval, as marked by 'all' in the table. In addition, when Hpo is larger than 4, the radar is inside the main oval from evening until late morning hours. The dayside main oval never reaches Tromsø latitude, and the radar is equatorward from the main oval from 9 to 18 MLT in all Hpo levels.

3 Statistical analysis results

3.1 Precipitation occurrence rate dependence on sunspot cycle, season, and MLT

As mentioned in Section 2.3, for a majority of the time the radar does not observe significant electron precipitation. Fraction of data points with auroral power larger than $2 \mathrm{~mWm}^{-2}$ for each year, month and MLT bin are shown in panels (d)–(f) of Figure 1. The radar data spans more than one and half solar cycles, from the peak of solar cycle 23 (January 2001) until the beginning of solar cycle 25 (April 2021), as shown in the sunspot number graph (red line) of panel (d). The histogram in panel (d) shows a clear solar cycle dependence in electron precipitation occurrence rate over Tromsø. The occurrence rate of auroral electron precipitation peaks at declining phases of the solar cycles.

Panel (e) of Figure 1 shows that electron precipitation is observed more frequently during autumn and spring than at mid-winter. The precipitation occurrence rate peaks at equinoxes in September and March. Both the solar cycle and seasonal dependence of the auroral occurrence rate will be discussed in detail in Section 4.1.

Panel (f) of Figure 1 shows auroral electron precipitation occurrence rate as function of MLT. The occurrence rate increases monotonically from post-noon to morning hours. A similar MLT trend in the occurrence rate of optical aurora was reported by Nanjo et al. (2022) who found that occurrence rate of the diffuse aurora increases monotonically from 18 MLT until 04 MLT, and decreases afterwards. An explanation for the observed MLT dependence of auroral electron precipitation occurrence rate will be given in Section 4.2.
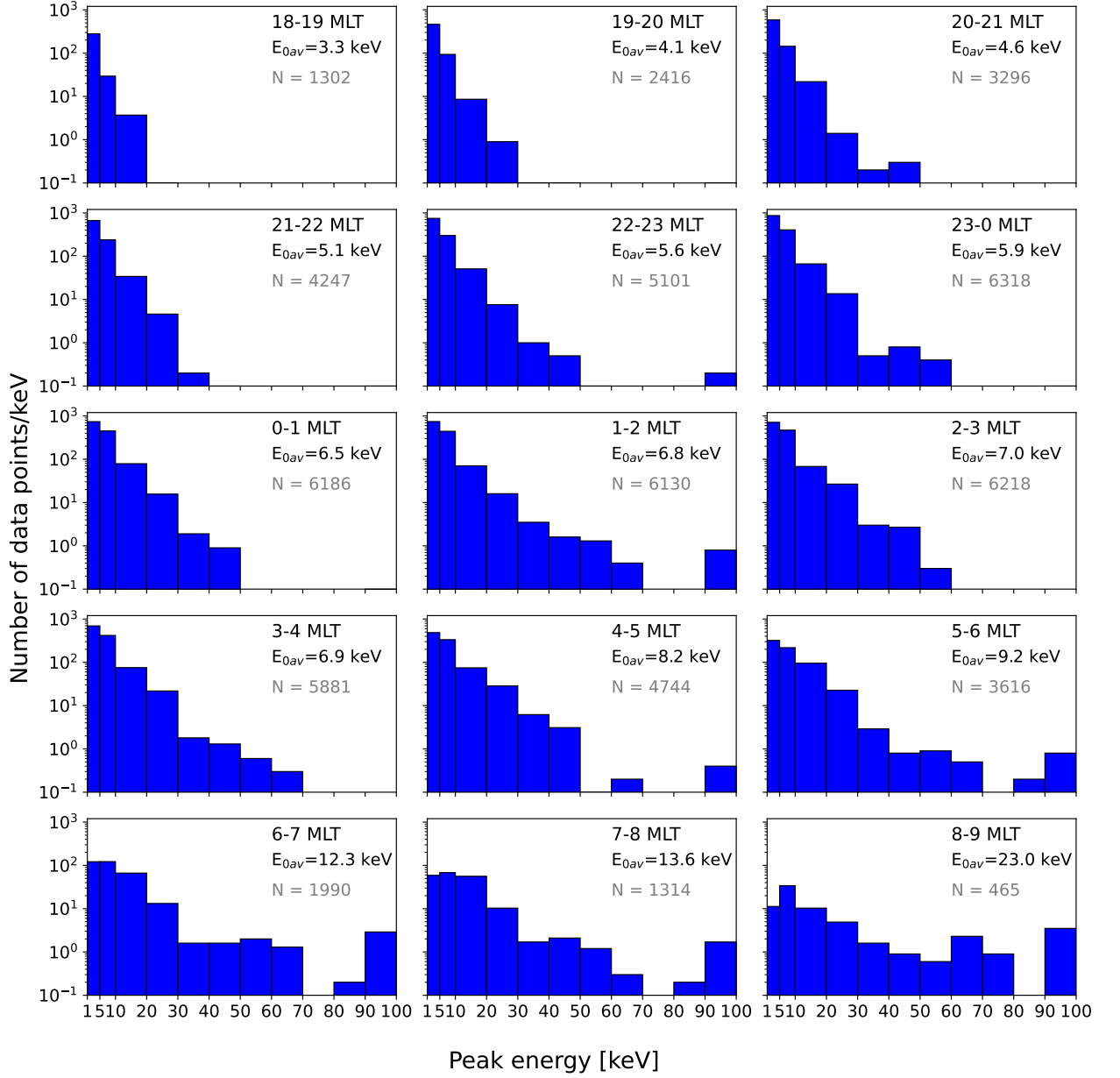
Figure 3. Distribution of peak energies in 1 h MLT bins. The average peak energy and total number of data points for each MLT bin are shown as shown as E_{0av} and N, respectively.

3.2 MLT dependence of peak energy, auroral power and number flux

To study the MLT dependence of peak energy, auroral power and number flux, we use the ELSPEC results with auroral power larger than 2 mWm^{-2} and zenith angle larger than 90°, and bin the data into 1-h MLT intervals from 18–09 MLT. The pre and post noon MLTs (10–18 MLT) are not included due to small number of data points (less than 500) in each MLT bin, as can be inferred from panel (c) of Figure 1.

Figure 3 shows distribution of the peak energy in units of counts per keV. The normalization allows us to use variable energy bin widths. The average peak energy for each
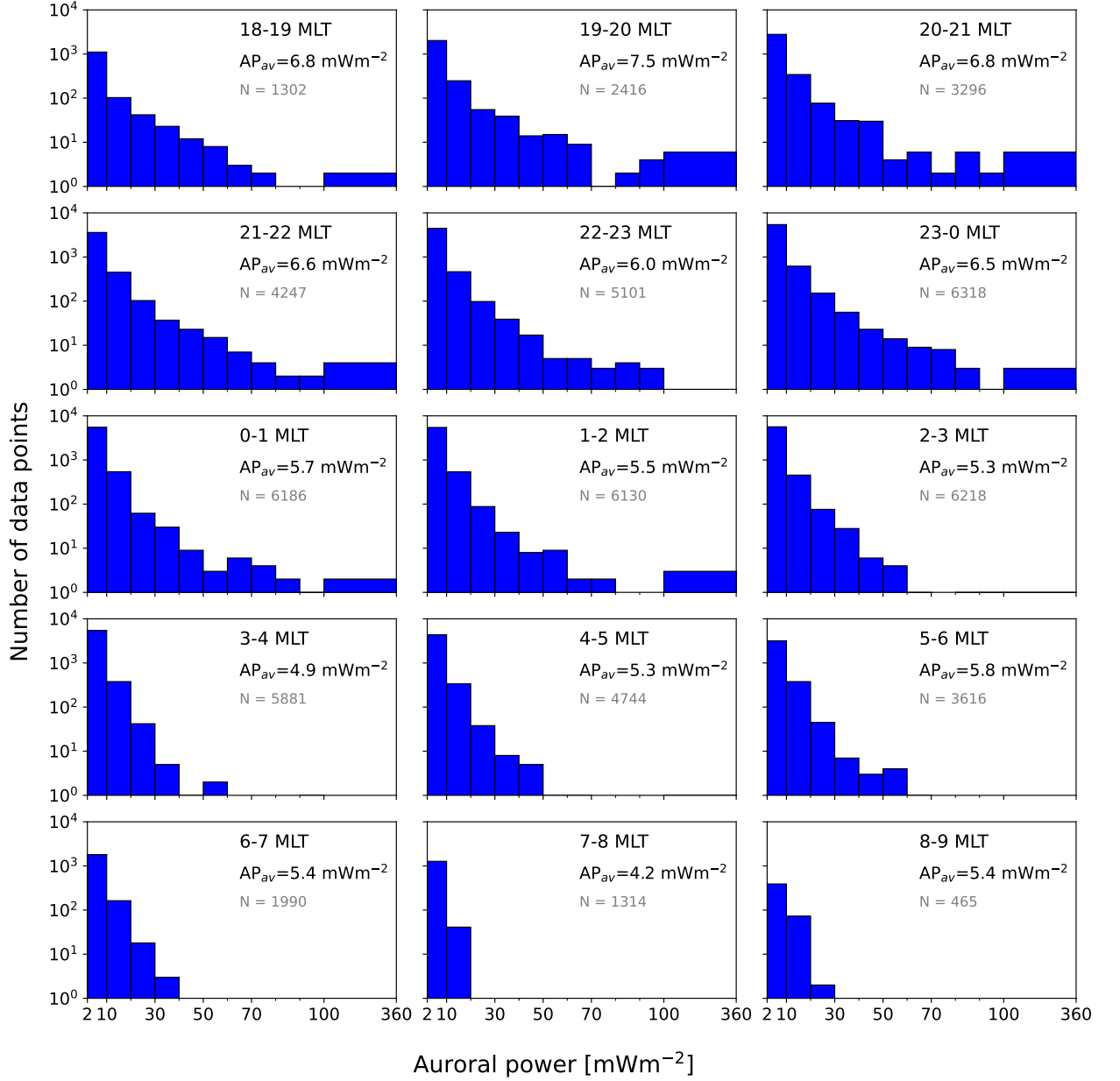
Figure 4. Distribution of auroral power in 1 h MLT bins. The average auroral power and total number of data points for each MLT bin are shown as shown as AP_{av} and N, respectively.

MLT bin is also shown in each panel as E_{0av}. The figure shows that 1–5 keV electrons dominate from the evening to the morning hours (18–06 MLT), while the 5–10 keV electrons dominate in the late morning hours, from 06 to 09 MLT. The average peak energy shown in the panels also increase almost monotonically with MLT, reaching above 10 keV after 06 MLT. The peak energy distributions become wider and extend to higher energies as one moves from the evening to the morning side of the auroral oval. For example, fraction of 10–20 keV electrons out of all detected precipitation increases from about 8% in the pre-midnight hours to about 15% in the post-midnight hours. The 30–100 keV peak energy bin also shows a significant increment, from below 0.5% to above 1%. While
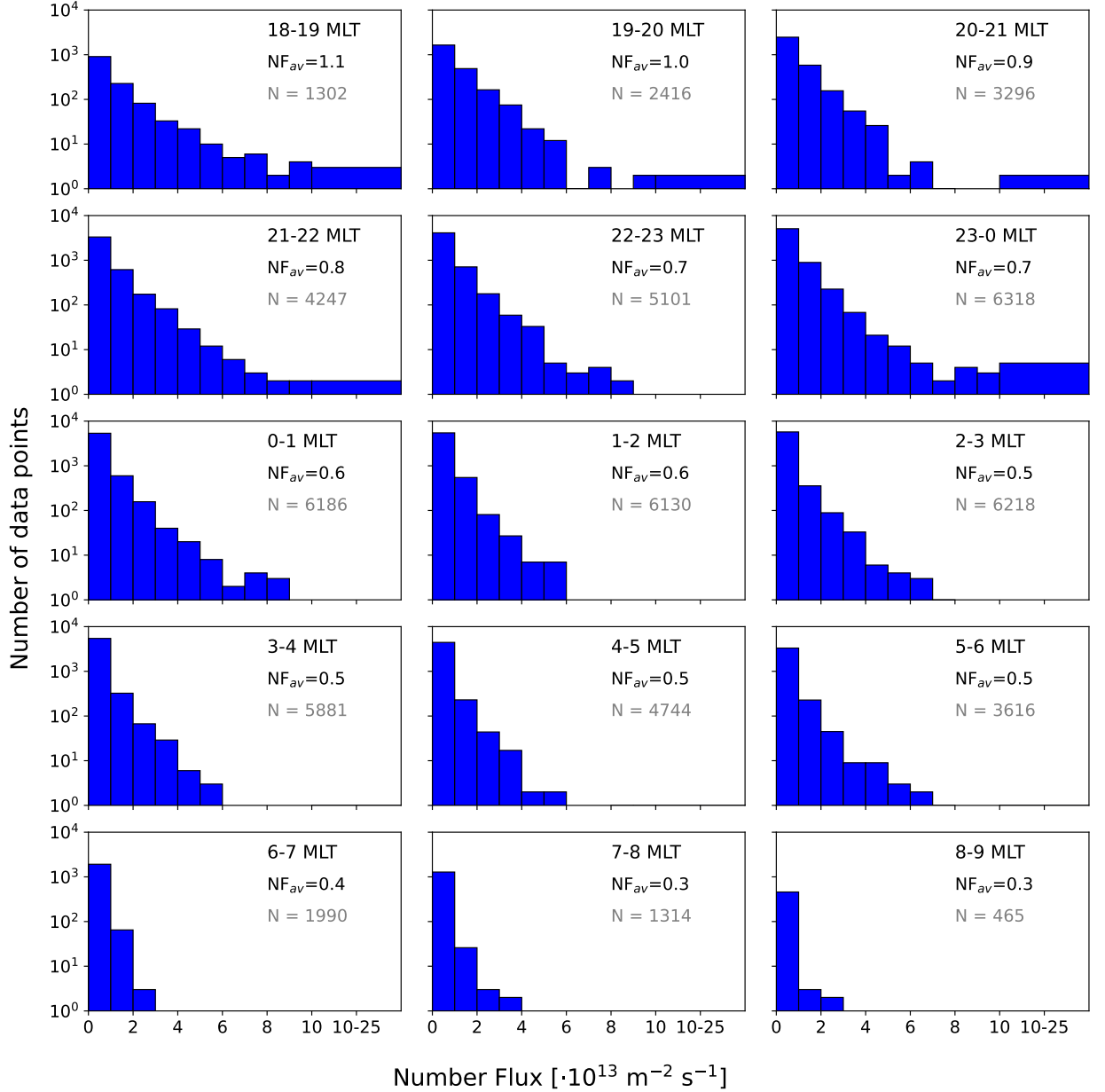
Figure 5. Distribution of number flux in 1 h MLT bins. The average number flux and total number of data points for each MLT bin are shown as shown as NF_{av} and N, respectively. NF_{av} is given in units $10^{13} m^{-2} s^{-1}$.

the largest observed energies in the evening hours are below 30 keV, the continuous distribution reaches 60 keV by 03 MLT and 80 keV by 09 MLT. In addition, the most energetic 90–100 keV electrons are clearly more common in the late morning MLT sectors.

Distributions of the auroral power and number flux are shown in Figures 4 and 5. The average auroral power AP_{av} and number flux NF_{av} are also shown in each panel for each MLT bin. The distributions are dominated by small auroral powers (2–10 mWm^{-2}) and number fluxes ($\leq 10^{13} m^{-2} s^{-1}$) at all MLTs. Contrary to the peak energy, the au-
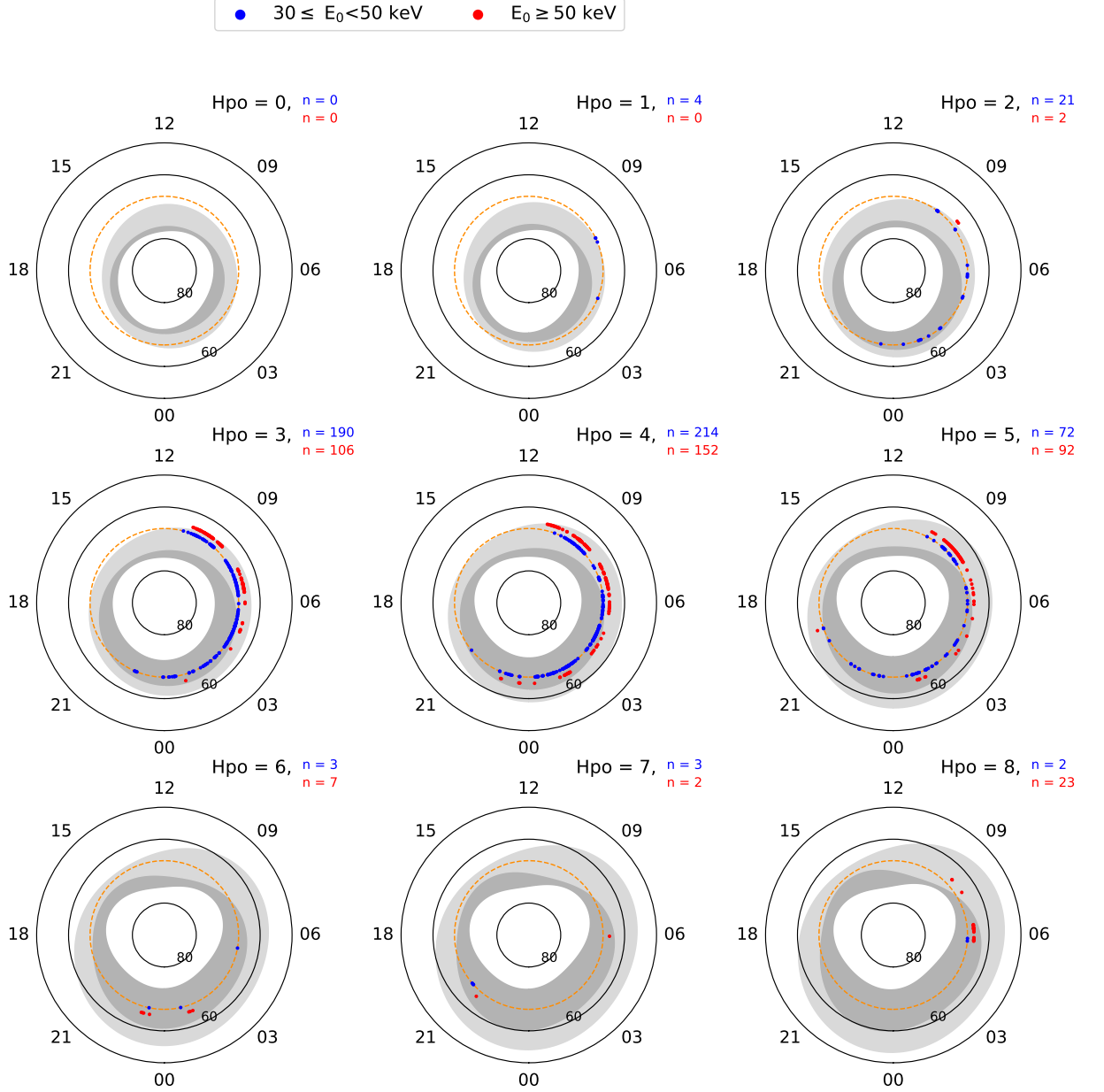
Figure 6. MLT distribution of high peak energies (E_0) in the auroral oval for different geomagnetic activity levels. Data points with peak energies 30–50 keV (50–100 keV) are shown as blue (red) dots in each oval plot. Number of data points for each category are given in the upper right corner of each panel. The main and diffuse ovals are shown as shades of dark and light gray.

roral power and number flux distributions are wider and extend to higher values in the pre-midnight hours than in post-midnight hours. For instance, the auroral power is larger than 30 mWm^{-2} in more than 2% of all detected precipitation before MLT midnight, but in only about 0.5% of the data after midnight. The largest auroral power obtained in this study, 360 mWm^{-2}, was also observed before midnight. The largest auroral powers detected in each MLT bin are at least 100 mWm^{-2} until 02 MLT, but the maximum power decreases to 60 mWm^{-2} by 06 MLT and below 30 mWm^{-2} by 09 MLT. In ad-
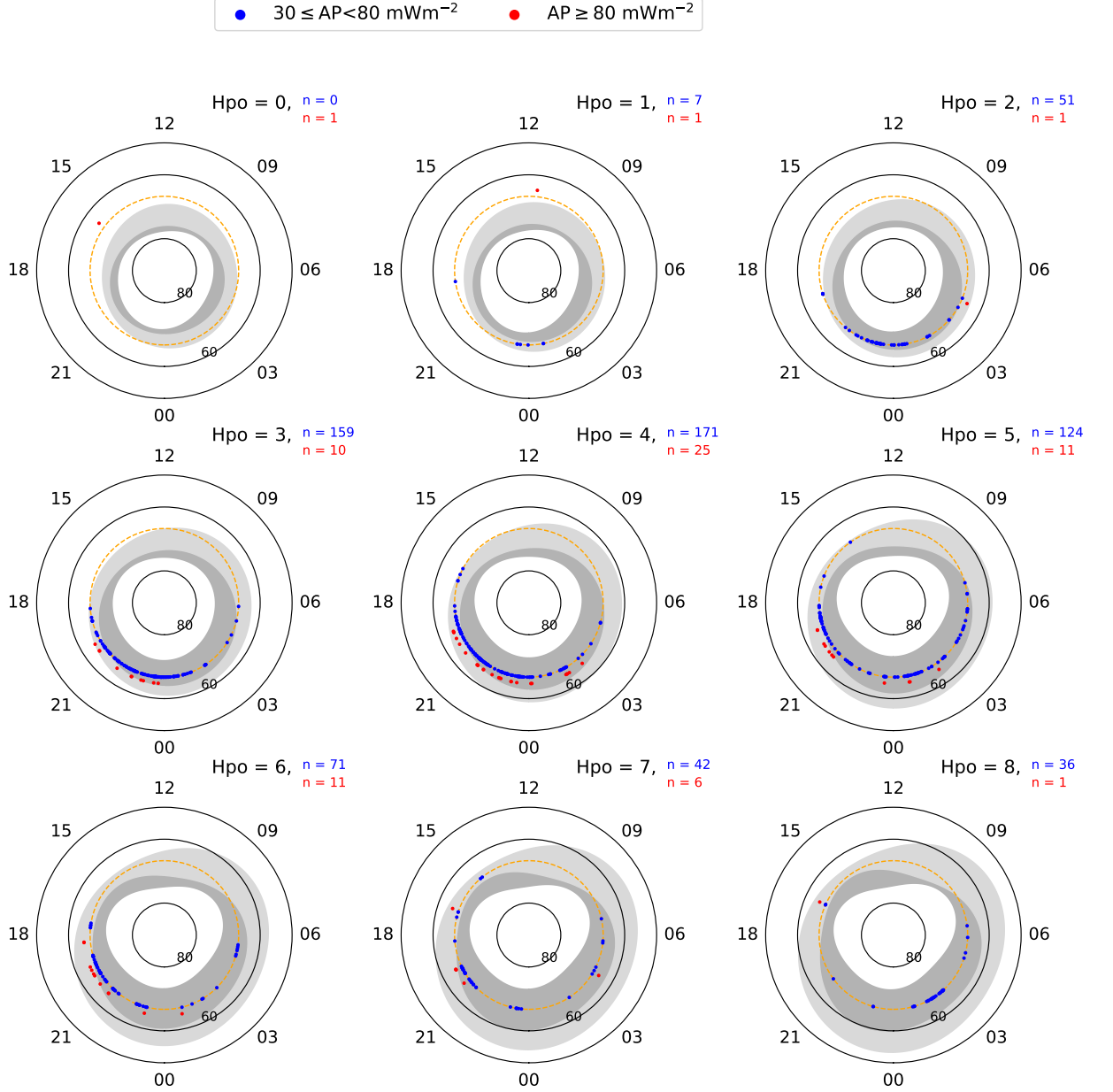
Figure 7. MLT distribution of large auroral powers (AP) in the auroral oval for different geomagnetic activity levels. Data points with auroral powers 30-80 mWm^{-2} ($\geq$ 80 mWm^{-2}) are shown as in blue (red) dots in each oval plot.

dition, the average auroral powers are all 6 mWm^{-2} and above in the pre-midnight hours, and below 6 mWm^{-2} in the post-midnight hours. Similarly, number fluxes larger than 10^{14} m^{-2}s^{-1} are measured during all pre-midnight hours except 22–23 MLT, but not at all after midnight, and the fraction of data points with total number flux larger than $4 \cdot 10^{13}$ m^{-2}s^{-1} decreases from more than 1% in the pre-midnight hours to 0.2% in the post-midnight hours. The average number flux decreases systematically from above 10^{13} m^{-2}s^{-1} at 18–19 MLT to about $3 \cdot 10^{12}$ m^{-2}s^{-1} in the late morning hours (7–9 MLT). One should note
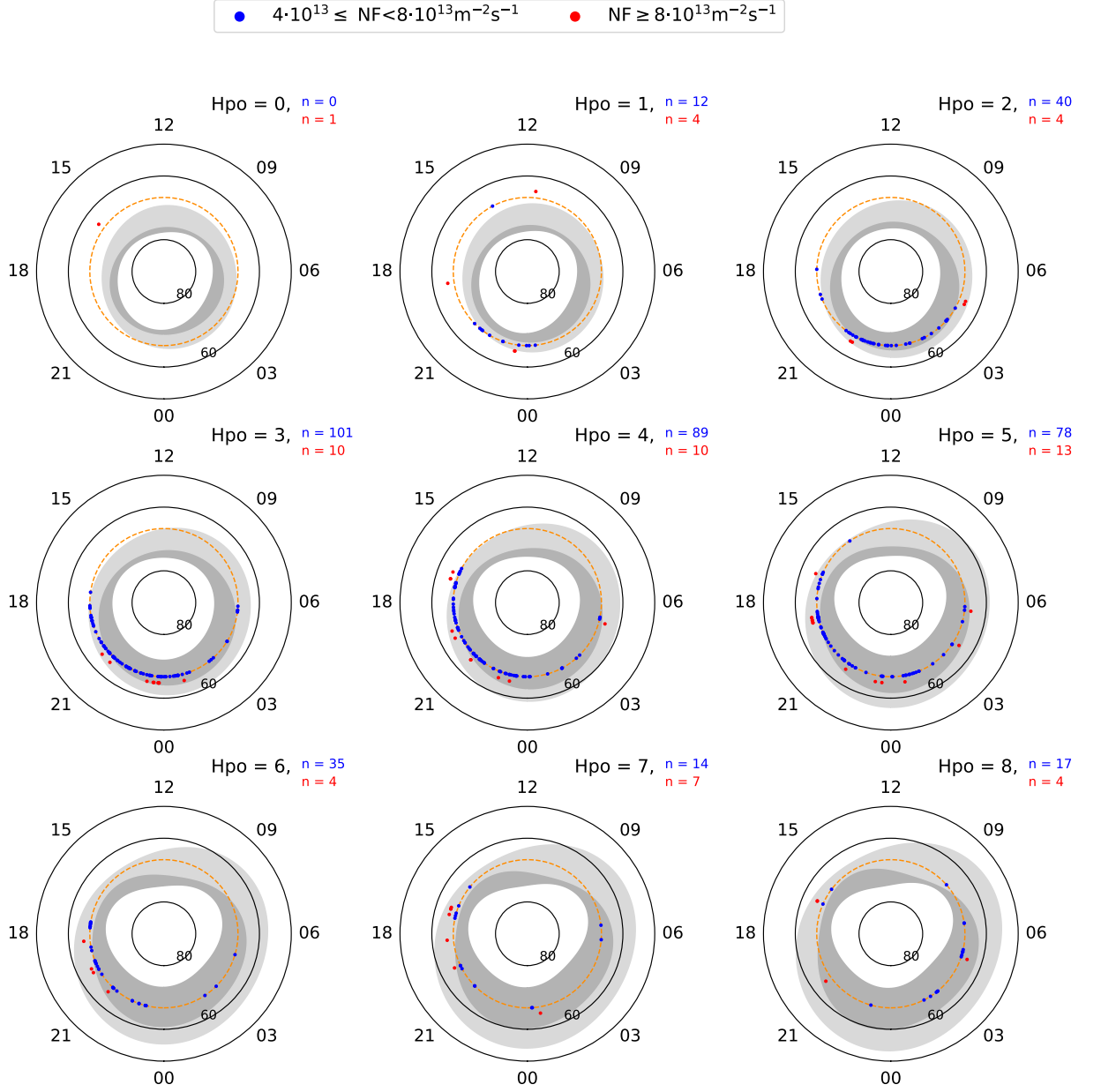
Figure 8. MLT distribution of large number fluxes (NF) in the auroral oval for different geomagnetic activity levels. Data points with number fluxes 4–8·10^{13} m^{-2}s^{-1} ($\geq 8 \cdot 10^{13}$ m^{-2}s^{-1}) are shown as in blue (red) dots in each oval plot.

309 that our analysis results cover only energies above 1 keV, which may affect the average
310 number fluxes, because the number flux may be significant below 1 keV.

Table 1. Hpo distribution of high peak energies (E$_0$ $\geq$30 keV), large auroral powers (AP$\geq$30 mWm^{-2}), and large number fluxes (NF$\geq$4$\cdot$10^{13} m^{-2}s^{-1}). From left to right, the first five columns are: Hpo value, total number of measurements, and occurrence rates of high peak energies, large auroral powers, and large number fluxes. The last two columns contain MLT intervals during which the radar is inside of the main oval, and inside the main or the diffuse ovals.

Hpo	N	E$_0$ $\geq$30 %	AP$\geq$30 %	NF$\geq$4$\cdot$10^{13} %	main oval MLT	main+diffuse ovals MLT
0	39832	0	0.003	0.003	–	23:00 − 05:00
1	112610	0.004	0.007	0.01	–	21:42 − 06:48
2	79614	0.03	0.07	0.06	21:36 − 04:18	20:00 − 10:18
3	57911	0.5	0.3	0.2	20:30 − 05:18	18:00 − 11:48
4	30046	1.2	0.7	0.3	19:18 − 07:30	16:12 − 13:00
5	11742	1.4	1.2	0.8	19:00 − 08:00	all
6	3965	—	—	—	18:42 − 08:12	all
7	1907	—	—	—	18:36 − 08:18	all
8	2134	—	—	—	18:30 − 08:18	all
$\geq$ 6	8006	0.5	2.1	1.0	—	—

3.3 Geomagnetic activity and MLT dependence of high peak energies, large auroral powers, large number fluxes, and the auroral oval location

Locations of the largest peak energies, auroral powers, and number fluxes in the auroral oval are shown in Figures 6, 7, and 8. The data are binned in nine groups according to the Hpo index. The lowest bin ("Hpo = 0" in the figures) corresponds to Hpo $\leq$ 0+, the second bin ("Hpo = 1") corresponds to 1− $\leq$ Hpo $\leq$ 1+, etc. The highest bin ("Hpo = 8") contains all data with Hpo $\geq$ 8−. Each plot shows the main (dark gray) and diffuse (light gray) auroral ovals calculated with the Feldstein-Starkov model. Individual data points are plotted at geomagnetic latitude of Tromsø and at the MLT of the measurement. The points are further divided into high (blue) and very high (red) values. The red dots are shifted slightly south from Tromsø for better visibility.

Locations of high peak energies are shown in Figure 6. The blue and red dots are high (30–50 keV) and very high (50–100 keV) peak energies, correspondingly. The figure indicates that vast majority of the high peak energy precipitation occurs after MLT midnight. With increasing geomagnetic activity level, more high-peak energy precipitation events are observed in the pre-midnight hours. Furthermore, very high ($>$ 50 keV) peak energies occur pre-dominantly during active geomagnetic conditions (Hpo $\geq$ 3). With increasing MLT the radar moves from the main oval to the diffuse oval, and the high peak energies are observed in the main oval before 06 MLT and in the diffuse oval after 06 MLT.

Locations of large auroral powers and number fluxes are shown in Figures 7 and 8, respectively. The blue dots correspond to large (30–80 mWm^{-2}) auroral powers in Figure 7, and to large (4–8 $\cdot$10^{13} m^{-2}s^{-1}) number fluxes in Figure 8. The red dots indicate very large auroral powers ($\geq$ 80 mWm^{-2}) and very large number fluxes ($\geq$ 8$\cdot$10^{13} m^{-2}s^{-1}), correspondingly. The oval plots indicate that majority of the large auroral powers and number fluxes are observed in the main auroral oval. The large values are observed from 18 MLT all the way until 06 MLT, with higher occurrence frequencies in the pre-midnight side of the main auroral oval. A few large values are measured also in the post-noon and early evening sides of the diffuse auroral oval. Auroral powers larger than 80 mWm^{-2}

and number fluxes larger than $8 \cdot 10^{13} \mathrm{m}^{-2} \mathrm{s}^{-1}$ are measured predominantly in the pre-midnight sector of the oval, and almost entirely during active geomagnetic conditions (Hpo ≥ 3).

Occurrence rates of high peak energies, large auroral powers, and large number fluxes, integrated over all MLTs, are shown in Table 1. For Hpo ≤ 5, the occurrence rates are calculated separately for each Hpo bin. For Hpo ≥ 6, the number of observed events in each Hpo bin is too small for accurate calculation of the occurrence rate. As a result, a single average occurrence rate is calculated for each quantity when Hpo is 6 and above, and shown in the last row of the table. MLT intervals during which the radar is inside of the main and diffuse ovals is shown in the last two columns. At Hpo values 0 and 1, Tromsø is always outside the main auroral oval and the occurrence rates are extremely small ($\leq 0.01\%$).

Occurrence rate of high peak energies ($E_0 \geq 30$ keV) increases monotonically from 0 at Hpo = 0 to 1.4% at Hpo = 5, but decreases to 0.5% when Hpo ≥ 6. As the total number of measurements for Hpo > 5 is small, the high Hpo bins may be affected by insufficient statistics. The radar data are also affected by expansion of the auroral oval with increasing Hpo. However, Hardy et al. (1985) reported that the average energy increases at Kp = 0–3 and remains constant at higher values of Kp, which has some similarity with our results.

Occurrence rates of large auroral powers (≥ 30 mWm^{-2}) and number fluxes ($\geq 4 \cdot 10^{13}$ m^{-2}s^{-1}) in Table 1 increase monotonically from zero at Hpo = 0 to 2.1% and 1.0% when Hpo ≥ 6, correspondingly. As large auroral powers and number fluxes are clearly concentrated in the pre-midnight side of the main oval of Figures 7 and 8, these trends may be connected to expansion of the main oval. This is discussed in more detail in Section 4.2.

3.4 Hpo dependence of peak energy, auroral power, and number flux

Because the radar beam is very narrow and auroras do not fill the whole auroral oval, the radar observes precipitation only for a fraction of time even in active conditions. To study the Hpo dependence of precipitation characteristics, we search for electron precipitation yielding the maximum auroral power during a 1-h time window, matching the time resolution of the Hpo index. For each 1-hour window, we then keep only one data point for which we have the values of peak energy, auroral power, and number flux.

Values of peak energy, auroral power, and number flux obtained as explained above versus the Hpo index in 3-h MLT intervals are shown in Figure 9. The blue and red dots are measurements from the main and diffuse ovals, correspondingly. The plots contain regression lines obtained from linear least squares fits to data points measured when Hpo ≤ 5. The slope (a) and intercept (b) of each regression line, together with their standard errors, are shown in the panels. The fits are not performed for data points measured when the Hpo index is above 5, because the small number of data points may not represent typical precipitation characteristics in these conditions.

The distributions of the blue (main oval) and the red (diffuse oval) data points clearly show how the radar moves with respect to the oval. In the 18–21 MLT bin the measurements are mostly from the diffuse oval, but also the main oval is observed when Hpo $>$ 2. Vast majority of the data are from the main oval from 21 to 03 MLT, with the diffuse oval observed only when Hpo < 3. In the morning side the radar again moves from the main oval to the diffuse oval, and majority of the data points are from the diffuse oval in the 06–12 MLT bin.

The peak energy fits in the left column of panels in Figure 9 show small positive slopes in all MLT sectors from 18 to 12. This is in line with the behaviour of the high peak energies in Table 1. The panels indicate that very high peak energies ($E_0 \geq 50$)
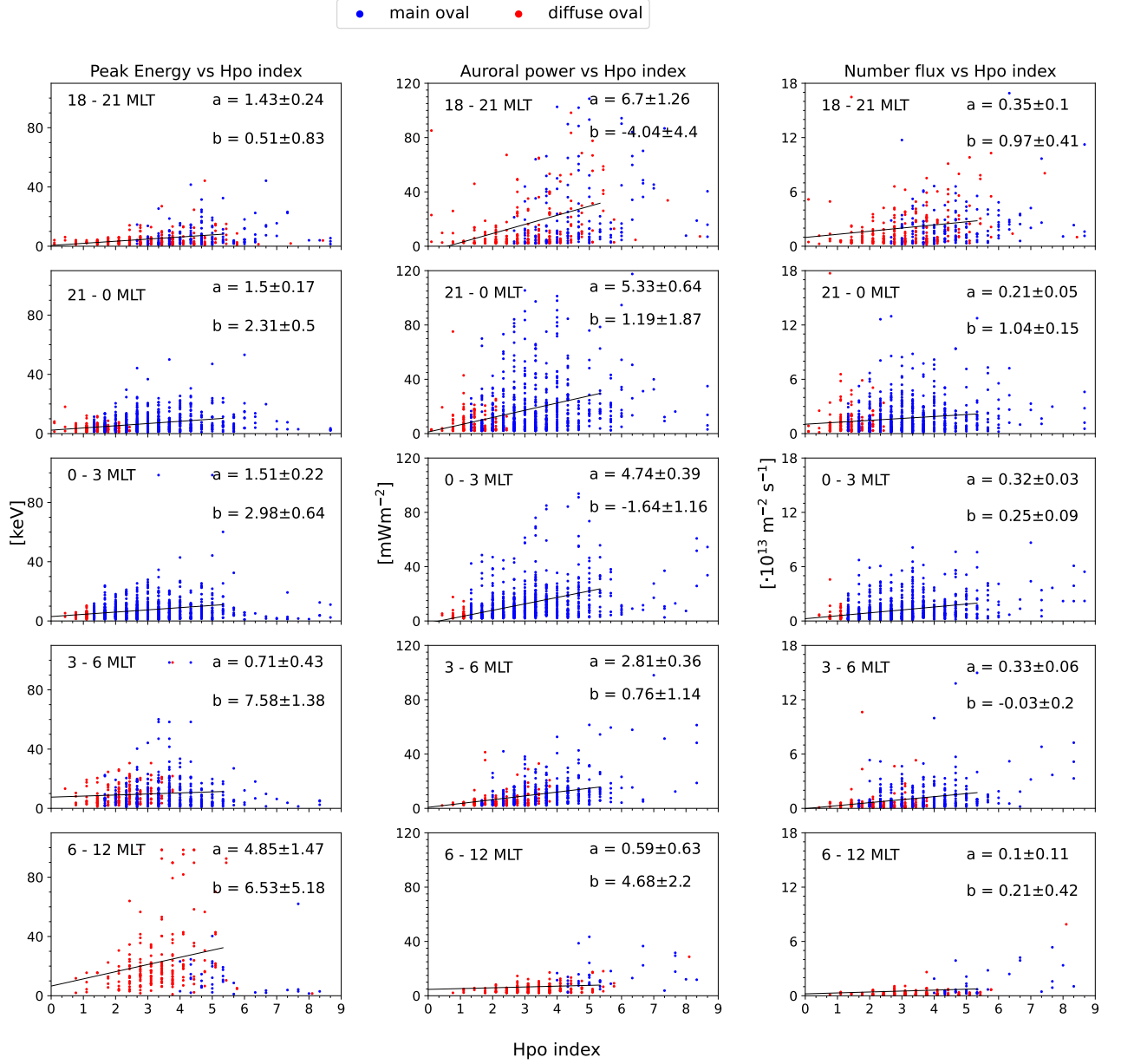
Figure 9. Peak energy (first column), auroral power (second column) and number flux (third column) versus the Hpo index. MLT intervals for each panel are marked on the upper left corner of each panel. The blue and red dots are measurements from the main and diffuse auroral oval, correspondingly. The lines are linear fits to data points measured when Hpo $\leq$ 5. The slope (a) and intercept (b) with their standard errors are given on the upper right corner of each panel. The data are maximum values in auroral power from 1-hour MLT bins, as explained in the text.

389 are not detected at the highest Hpo values but they are common at Hpo values 3–6. The
390 highest slope in the linear fit is observed in the late morning and pre-noon hours. The
391 positive intercepts in the linear fits indicate that the peak energy does not drop to zero
392 even in quiet conditions.

The auroral powers in the middle panels show stronger Hpo dependence than the peak energies. The steepest slopes are found from the pre-midnight and evening hours where discrete aurora dominates. Also these fits are in line with the Hpo dependence of the largest auroral powers in Table 1. Similar behaviour is seen also in the number fluxes on the right, but the slopes are clearly smaller than for the auroral power. Finding the strongest correlations with Hpo in the auroral power is in line with the results of Hardy et al. (1985), who reported an increase in AP but constant E_0 with increasing values of Hpo.

As can be easily seen from Figure 9, the data points are highly scattered although positive correlations were found. This is confirmed also by correlation coefficients, which are below 0.5 for all quantities in all MLT bins. The small correlations may be expected, as Hpo is a global index, while the radar makes extremely localized measurements. Previous studies have also shown a non-linear relationship between the Hpo index and hemispheric auroral power (Newell & Gjerloev, 2011; Zhang & Paxton, 2008).

4 Discussion

4.1 Solar cycle and seasonal variations in precipitation occurrence rate

The histogram in Figure 10, also shown in panel (d) of Figure 1, shows solar cycle variations of the auroral occurrence rate. The red line shows the sunspot number and one can see that the electron precipitation occurrence rate peaks in the declining phases of solar cycles 23 and 24. In addition, the fraction of data points for which the Hpo index is larger than 2 is shown by a blue line in the figure. The peaks of yearly precipitation occurrence rates in 2002–2004 and 2015–2017 match with the peaks in the Hpo > 2 curve. Previous studies have also reported maximum Kp index in the declining phases of solar cycles (e.g., Matzka et al., 2021).

As discussed in Section 2.4, the auroral oval expands to Tromsø latitude only when Hpo is above 2, and as will be discussed in Section 4.2, precipitation rarely occurs outside the Feldstein-Starkov oval. The solar cycle (sc) variation in our data is thus most likely due to the solar cycle variation in magnetic activity, which controls the auroral oval location, width and occurrence rates of precipitation. It implies that the auroral precipitation occurrence rate peaks at Tromsø in the declining phases of the solar cycle because the oval is more often above Tromsø at these times. The highest auroral occurrence frequency obtained in our study is about 32% in year 2002, which is in the declining phase of solar cycle 23. Both the sunspot number and geomagnetic activity (in terms of Hpo index) were greater during sc 23 than sc 24, and we see the same effect in the occurrence rate of auroral electron precipitation in Tromsø.

Similar solar cycle dependence in the auroral occurrence rate has been reported in optical aurora at the same location by Nanjo et al. (2022), who used 10 years of all sky camera data from 2011 until 2021. In their study, the optical aurora occurrence rate at Tromsø shows maxima at the declining phase of sc 24 with maximum of 70% in year 2015. The authors calculated the 2015 occurrence frequency by including months January-March from year 2016, which accounts more than 50% of the data in their calculation. In our study, we obtained maximum occurrence frequency of about 21% in year 2016 in sc 24. Since the 2015 result of Nanjo et al. (2022) contain data from year 2016, it seems that the year of maximum occurrence rate in our study match with the optical aurora occurrence rate.

The lower occurrence frequency obtained in our study is obviously due to the very narrow field–of–view (FoV) of the radar beam as compared to that of the all sky camera. The all sky camera FoV covers an area about 750 km in diameter, and the radar covers only an area about 1 km in diameter, both at 100 km altitude. Due to its large
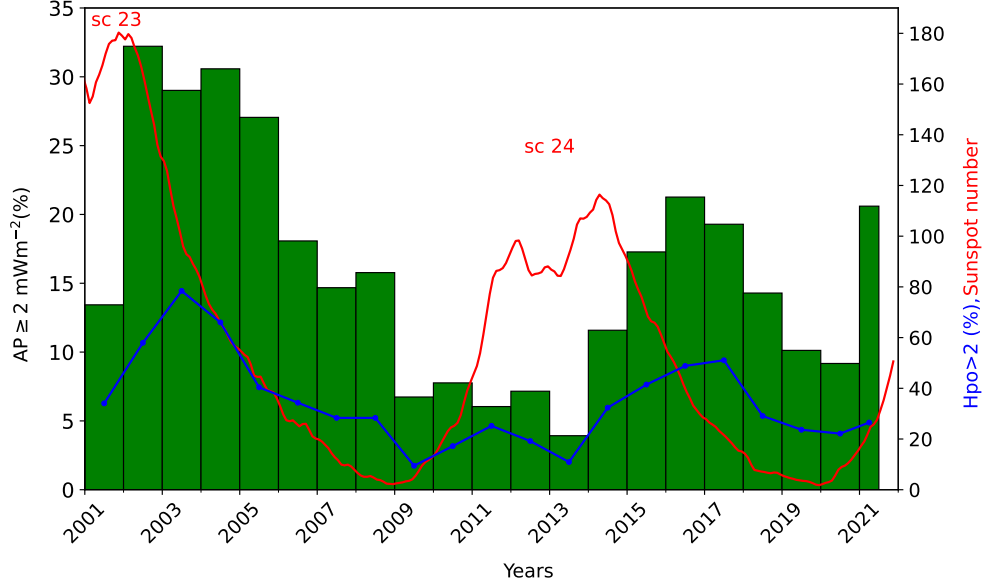
Figure 10. Solar cycle and geomagnetic activity variation of auroral electron precipitation occurrence rate in Tromsø. The red and blue lines show the sunspot number and the percentage of data points with Hpo > 2, correspondingly.

FoV, the all-sky camera has a higher probability of capturing auroral structures that occur in different geomagnetic activity conditions.

Regarding global occurrence rate of aurora, using intense (> 5 mWm^{-2}) electron precipitation measurements of DMSP satellite, Newell et al. (1998) found that the total number of intense aurorae is uncorrelated with solar activity in darkness, but is negatively correlated with solar activity in sunlit conditions. Using data from the FAST satellite, Cattell et al. (2013) found minima in the auroral occurrence rate at solar maxima both in sunlit and darkness conditions.

In Section 3.1, we briefly described monthly variation of the auroral occurrence rate shown in panel (e) of Figure 1. As shown in the figure, the auroral occurrence frequency has maxima during equinoctial months, in September and March, and a minimum in December to January. Nanjo et al. (2022) found maximum optical auroral occurrence frequency in October and February, and minimum in December. The semi-annual variation in geomagnetic activity has long been recognized (Cortie, 1912; Chapman & Bartels, 1940; Russell & McPherron, 1973) and it gives peaks in geomagnetic activity at times close to equinoxes. As Lockwood et al. (2020) show, the semi-annual variation is almost entirely due to the Russell–McPherron (R–M) effect. According to the R–M effect (Russell & McPherron, 1973), the probability of southward interplanetary magnetic field (IMF) increases during equinoxes, because the IMF B_Y component on the solar equatorial plane in the Geocentric Solar Equatorial (GSEQ) frame gives a component to the north–south B_Z component in the Geocentric Solar Magnetospheric (GSM) frame. Southward IMF in the GSM coordinate system increases the coupling between the IMF and the magnetosphere providing energy for geomagnetic storms and substorms (Newell et al., 2007).
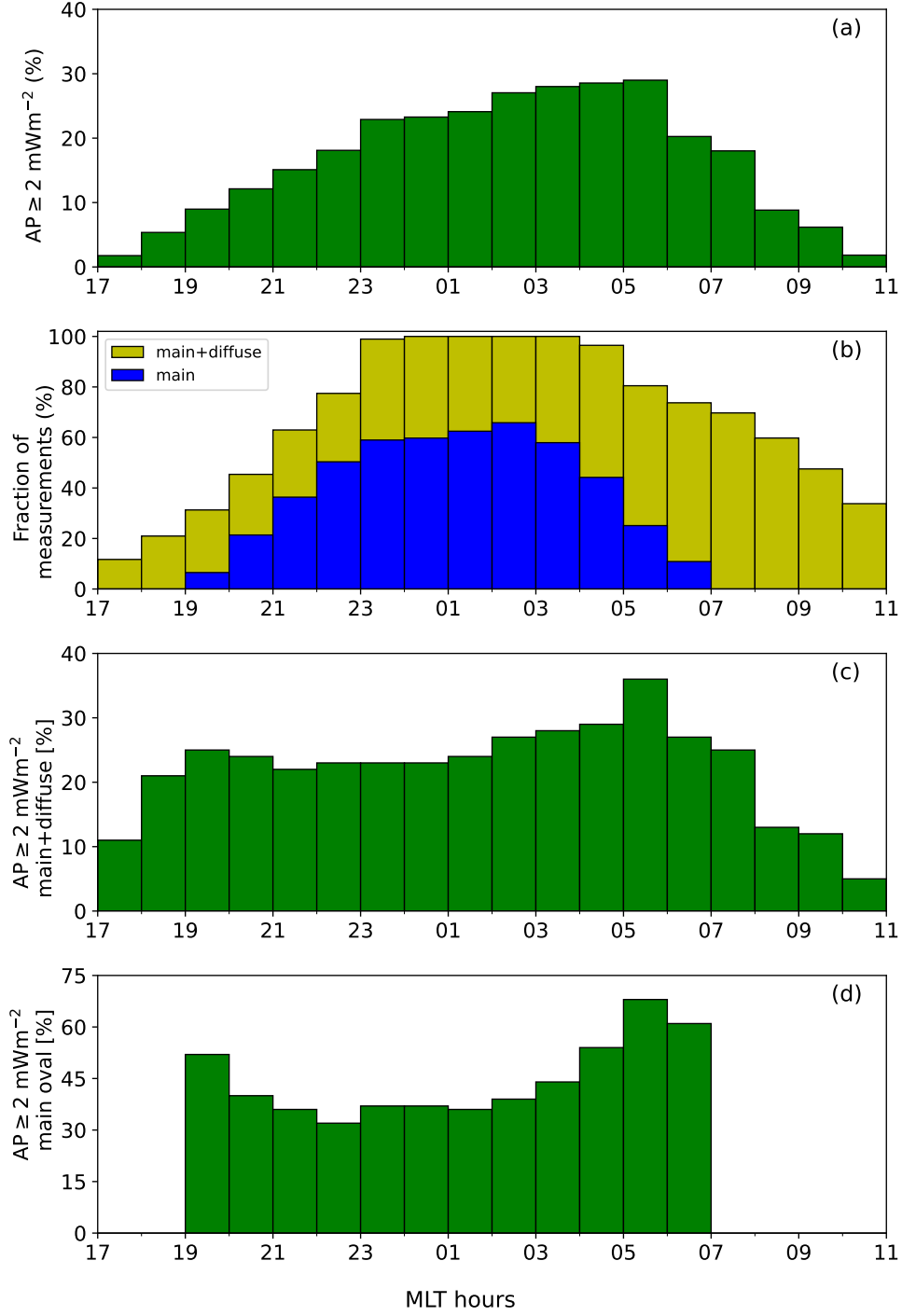
Figure 11. Panel (a): MLT distribution of electron precipitation occurrence rate in Tromsø. Panel (b): Fraction of data points measured in the main (blue), and in the main+diffuse oval (yellow). Panels (c) and (d): MLT distribution of electron precipitation occurrence rate in the main+diffuse oval, and in the main oval, respectively. The 17–19 and 07–11 MLTs are not shown in panel (d) because we do not have sufficient statistics (N<500).

4.2 MLT variations in precipitation occurrence rate

The motion of the auroral oval boundaries with increasing Hpo index was presented in Section 2.4. Here we discuss its implications to the radar measurements and to interpretation of our results. We obtain the electron precipitation occurrence rate by calculating the fraction of data points (in percent) with auroral powers larger than 2 mWm^{-2}. The precipitation occurrence rate as function of MLT, as observed by the radar, is shown in panel (f) of Figure 1 and is reproduced for 17–11 MLT in panel (a) of Figure 11. The histogram in Figure 11 of panel (a) shows a monotonic increase in precipitation occurrence rate with MLT, from below 5% in 17–18 MLT to about 30% in 05–06 MLT.

Panel (b) of Figure 11 shows the fraction of measurements that are from the main and diffuse ovals as function of MLT. This fraction increases with MLT and reaches almost 100% at 23 MLT. From 23 until 04 MLT, the radar is almost always inside the main or diffuse oval, and inside the main oval for more than 50% of the time. After 06 MLT, the fraction of data points measured in the main oval decreases significantly and drops almost to zero by 08 MLT. However, the radar is inside the diffuse oval for a significant fraction of time until 11 MLT.

Precipitation occurrence rate calculated from data points measured when the radar is within the auroral oval (main or diffuse) is shown in panel (c) of Figure 11. This distribution does not show the monotonic increase with MLT, but the occurrence rate is rather stable from 18 to 02 MLT with a small local maximum centred at 19–20 MLT. A more pronounced maximum between 02 and 07 MLT that peaks at 05–06 MLT is seen in the morning side. The monotonic increase in the total precipitation occurrence rate in panel (a) is thus caused by the increasing fraction of time the radar spends within the oval. However, the morning side maximum cannot be explained by this mechanism. The precipitation occurrence rate in the whole (main and diffuse) oval is 20–25% from 18 to 02 MLT, and reaches 35% in the morning side maximum at 05–06 MLT.

Precipitation occurrence rate for the main oval alone is shown in panel (d) of Figure 11. The occurrence rate reaches higher than 50% during evening (19–20 MLT) and morning (04–08 MLT) hours, attaining maximum of close to 70% in the 05–06 MLT sector. Close to midnight, 21–02 MLT, the occurrence rate is about 35%. Particularly, the radar observes the main oval in the early evening hours (19 MLT) only when the Hpo index is 5 and above, as indicated by Table 1. In addition, it is only when the Hpo index is 4 and above that the morning side of the main oval (the 05–08 MLT sector) expands to the latitude of the radar beam. Hence, the radar observes the evening and morning sides of the main oval only during active geomagnetic conditions which might produce the evening and morning maxima in panel (d) of Figure 11.

Therefore, we can conclude that the increase of occurrence rate of auroral precipitation with MLT in the evening and pre-midnight sectors (Figure 11 a) comes from the motion of Tromsø under the auroral oval. When Tromsø is located within the main auroral oval, the highest occurrence rates of auroral precipitation are obtained. During evening and midnight, the occurrence rates are smaller than for all-sky camera (ASC) observations at the same location, but in the morning main oval, typically filled with diffuse precipitation, the values reaching 70% are close to values reported by Nanjo et al. (2022) from ASC measurements. As showed byNewell et al. (2009), the evening side of the oval is dominated by discrete monoenergetic electron precipitation, which is harder to capture by a narrow FoV radar than the morning side diffuse precipitation.

4.3 The peak energy, auroral power, and number flux statistical analysis results

As shown in Figure 3, the average energy grows almost monotonically with MLT reaching values larger than 10 keV after 6 MLT. This is in accordance with earlier stud-

515 ies. For example, Hardy et al. (1985) found that within 50 eV to 20 keV energy range,
516 the average electron energies are highest on the morning side of the oval. Cai et al. (2013)
517 showed that the height-integrated Hall-to-Pedersen conductance ratio, which is a proxy
518 for the average energy of the precipitation (Robinson et al., 1987), grows with MLT, has
519 a maximum within 03–06 MLT for Kp< 3- and shifts to 06–09 MLT for higher Kp val-
520 ues.

521   Regarding energetic electron precipitation (with peak energies higher than 30 keV),
522 we found that it occurs primarily in the post-midnight and morning sides of the auro-
523 ral oval (Figure 6), with expansion towards midnight and pre-midnight hours during ac-
524 tive conditions (Hpo $\geq$ 3). This is in agreement with earlier studies; for example, us-
525 ing NOAA POES data, Lam et al. (2010) showed that the number flux of > 30 keV elec-
526 trons significantly increases during active geomagnetic conditions and it is maximum in
527 the dawn sector outside of the plasmapause. Electrons with energies in the range of 30–
528 100 keV are absorbed in the atmosphere typically between 70 and 100 km altitudes and
529 they produce cosmic noise absorption (CNA). Measurements of CNA near the magnetic
530 latitude of Tromsø show a morning maximum followed by a minimum close to dusk (Kavanagh
531 et al., 2004; Grandin et al., 2017). Furthermore, Grandin et al. (2017) found that CNA
532 associated with substorm activity dominates in the 21–06 magnetic local time (MLT)
533 sector.

534   Morning sector electron precipitation is known to be associated with diffuse aurora,
535 including pulsating aurora, (Newell et al., 2009; Nanjo et al., 2022). Medium-energy (1–
536 30 keV) electrons are injected into the inner magnetosphere during periods of enhanced
537 convection or substorms. During the eastward drift motion, wave-particle interactions
538 scatter the electrons into the loss cone and the most likely mechanism for electrons in
539 the morning sector is whistler mode chorus waves (Lam et al., 2010; Thorne et al., 2010,
540 2021). These chorus waves are also capable of scattering trapped high-energy (hundreds
541 of keV) radiation belt electrons into the loss cone.

542   In the evening and pre–midnight sectors, the distributions of peak energies max-
543 imize in the 1–5 keV bin, and the average peak energies are about 5 keV. As Newell et
544 al. (2009) showed, this region is dominated by so-called monoenergetic electron fluxes,
545 which are most likely generated in the auroral acceleration region (Carlson et al., 1998;
546 Aikio et al., 2002; Paschmann et al., 2003). Examples of these so called inverted-V elec-
547 tron spectra are shown in Tesfaw et al. (2022).

548   The average auroral power shwon in Figure 4 is somewhat higher before magnetic
549 midnight (6.0–7.5 mWm^{-2}) than after midnight (4.2–5.7 mWm^{-2}), which is in agree-
550 ment with Newell et al. (2009) who conclude that the energy flux is dominated by night-
551 side, particularly pre-midnight. Large auroral powers (≥ 30 mWm^{-2}) in our study are
552 observed predominantly in the pre-midnight sector of the main auroral oval. The power
553 is carried by large number fluxes of ≤ 5 keV electrons. The largest auroral powers (≥ 80 mWm^{-2})
554 occur only in the evening to midnight sector and are not observed after 2 MLT even dur-
555 ing high geomagnetic activity. However, large auroral powers between 30 and 80 mWm^{-2}
556 expand toward morning sector when Hpo ≥ 4 (Figure 7).

557   Our results of average power being somewhat larger before midnight than after mid-
558 night may seem partially contradictory to the results by Hardy et al. (1985), who found
559 that the region of maximum energy flux is close to magnetic midnight, and moves from
560 pre-midnight to post-midnight with increasing Kp. However, Hardy et al. (1985) stud-
561 ied averaged auroral powers, which include also the regions with no or very little pre-
562 cipitation, while we have included only data with auroral power > 2 mWm^{-2} in our study.
563 This effectively increases our average powers in the evening side where discrete aurora
564 dominates, while the effect is smaller in the morning side diffuse precipitation region. An
565 additional factor may be that the radar observes the evening sector main oval only in

active conditions, when the auroral powers are typically high, while the midnight and morning sectors of the oval are reached already at lower activity levels.

The number flux (Figure 5) and auroral power distributions are very similar with each other in our study. We observe large number fluxes ($>4 \cdot 10^{14}$m^{-2}s^{-1}) predominantly in the evening and pre-midnight hours, and the average total number fluxes decrease from evening to morning MLTs. In the study by Newell et al. (2009), large number fluxes and auroral powers occur within the same regions in the afternoon to night sector for mono-noenergetic and broadband aurora, though number fluxes seem to maximize at a bit earlier MLT than auroral powers for monoenergetic aurora. Number fluxes of diffuse precipitation in the midnight and morning sectors are about as high as number fluxes in the evening and pre-midnight sectors both by Hardy et al. (1985) and Newell et al. (2009), and the difference to our observations can be due to the same reasons as we discuss above for auroral powers.

We found that auroral power, number flux and peak energy all increase with the Hpo index to Hpo values about 4–5 (Figure 9). Increase of auroral power and number flux with increasing geomagnetic activity has also been observed using satellite measurements (Hardy et al., 1985, 1991; Zhang & Paxton, 2008; Vorobjev et al., 2013; Yakovchuk & Wissing, 2019). Hardy et al. (1985) found that the average energy increased with Kp for Kp = 0–3, and remained constant for higher Kp values. Hence, our results seem to be in a qualitative agreement with Hardy et al. (1985), but insufficient statistics for high Hpo values in our data may contribute to the result.

4.4 Limitations of the ELSPEC analysis

ELSPEC is nominally using data from 80-150 km altitudes, and covers 1–100 keV energies. These limitations arise from the complex ion chemistry below 80 km altitude, and from the significant fraction of the long-lived O^+ ions above 150 km. We have also limited ourselves to auroral powers larger than 2 mWm^{-2} to avoid very low electron densities and noisy data. Since all radar operation modes do not provide data down to 80 km altitude, we have truncated some of the energy spectra according to the lowest measured altitude, as explained in Section 2.2. While 80% of the electron density profiles reach down to 83 km altitude, which is typically enough to cover the whole 1-100 keV energy range, 20% of the profiles reach only down to 93 km altitude, which corresponds to about 40 keV electrons. Our occurrence rates for 40–100 keV electrons may thus be underestimated by up to 20% due to limitations of the radar operation modes.

Temporal resolution of our data is close to 1 min which is not sensitive enough for auroral structures that vary in time-scales of a few seconds (Tesfaw et al., 2022) or down to sub-second level (Dahlgren et al., 2011). The long integration of the radar data may thus have smoothed out rapid variations and short-lived maxima in peak energy, auroral power, and number flux. A general property of the radar observations is also that auroral power is underestimated when the radar beam is not uniformly filled by the precipitation (Tesfaw et al., 2022). We thus have a reason to believe that our auroral powers and number fluxes may be slightly underestimated, especially in active conditions.

We assume the electron density enhancements to be produced solely by electron precipitation. However, ion precipitation may produce ionization especially in the dusk-midnight side of the auroral oval (Hardy et al., 1989; Newell et al., 2005; Wissing et al., 2008), and its effect might have been interpreted as electron precipitation in our analysis. The ion energy flux is largest around 18 MLT close to equatorward boundary of the electron precipitation, where the ion energy flux can be equal or slightly exceed the electron energy flux (Hardy et al., 1989), while its contribution is much smaller in other latitudes and MLTs. Our results may thus be affected by the ion precipitation in the evening MLT sector when Hpo = 2–4, which are the conditions when Tromsø is close to the equa-

torward boundary of the oval close to 18 MLT. In other MLT sectors and Hpo levels the ion energy flux is expected to be well below that of the electrons.

5 Conclusions

We have used 20 years of the EISCAT UHF radar data from years 2001–2021 to study the statistical characteristics of 1–100 keV electron precipitation over Tromsø at 66.7° MLAT. The ELSPEC software (Virtanen et al., 2018) yields us the peak energies, auroral powers and number fluxes of precipitating electrons from field-aligned electron density profiles for solar zenith angles larger than 90°. Our study includes the 30–100 keV energetic electrons that have been poorly covered in previous satellite studies. In order to put the local measurements into a more global context, we use the empirical Kp dependent Feldstein-Starkov model of the auroral oval location (Starkov, 1994).

We found that occurrence rate of electron precipitation in Tromsø peaks during the declining phases solar cycles, in 2002–2004 for sc 23 and in 2015–2017 for sc 24. The occurrence rate variations match with those of Hpo > 2, indicating that they are caused by solar cycle variations in geomagnetic activity. The highest auroral occurrence frequency obtained in our study is about 32% in year 2002 of sc 23. Both the sunspot number and geomagnetic activity were greater during sc 23 than sc 24, and we see the same effect in the occurrence rate of auroral electron precipitation in Tromsø.

We also found a clear seasonal variation, with the electron precipitation occurrence rate being maximum during equinoctial months of March and September and minimum in December and January. This is most likely due to the Russel–McPherron effect (Russell & McPherron, 1973).

The MLT variation of electron precipitation occurrence frequency in Tromsø increases continuously from evening to morning MLTs, from below 5% in the 17–18 MLT sector to about 30% in 05–06 MLT sector. The MLT variations are caused mainly by the motion of the radar site with respect to the auroral oval as the Earth rotates under the oval. On the average, the fraction of time when the radar is located within the oval increases from 17 to 23 MLT. The radar is almost always inside the auroral oval from 23 to 04 MLT, after which the fraction of time spent within the oval decreases with MLT. The precipitation occurrence rate in the oval peaks at 05–06 MLT.

To study the true MLT dependece of auroral electron precipitation, we estimated the occurrence frequency of precipitation including only those times when Tromsø was located within the main Feldstein-Starkov oval. The occurrence rate reaches higher than 50% during evening (19–20 MLT) and morning (04–08 MLT) hours, attaining a maximum value 70% at 05–06 MLT. During evening and midnight hours, the occurrence rates of electron precipitation observed by the radar are smaller than occurrence rates of optical aurora observed by the all-sky camera (ASC) at the same location, but in the morning oval the values are close to those reported by Nanjo et al. (2022) from ASC measurements. Due to the narrow radar beam width (0.6°), discrete electron precipitation structures are often missed by the radar in the evening sector, but the morning sector is typically filled with diffuse precipitation covering a large area.

The energy spectra of precipitating electrons become harder as one moves from the evening to morning, in accordance with earlier satellite studies. The peak energy distribution is dominated by 1–5 keV energies from dusk to dawn (18–06 MLT), and by 5–10 keV energies in the 06–09 MLT sector. Energetic ≥ 30 keV electrons precipitate most frequently after magnetic midnight, but in active conditions (Hpo > 4), the energetic precipitation expands also to the pre-midnight MLTs. Peak energies higher than 50 keV are observed exclusively after 22 MLT. Energetic electrons observed in Tromsø precipitate mostly in the main auroral oval before 06 MLT, and in the diffuse oval after 06 MLT.

The analyzed auroral power and number flux distributions are very similar with each other. Small auroral powers (2–10 mWm^{-2}) dominate the auroral power distribution at all MLTs. Large auroral powers ($\geq$30 mWm^{-2}) are measured mostly in the evening and pre-midnight MLTs in the main auroral oval and they are carried by large number fluxes of ≤ 5 keV electrons. The largest auroral powers (≥ 80 mWm^{-2}) occur only in the evening to midnight sector and are not observed after 2 MLT even during high geomagnetic activity.

Finally, we found that auroral power, number flux and peak energy all increase with the Hpo index to Hpo values about 4–5, which is in qualitative agreement with Hardy et al. (1985), who reported increase until Kp value 3. Insufficient data statistics for higher geomagnetic activity levels prohibit us from making a definite conclusion whether the dependence breaks down for high Hpo values.

References

Aikio, A. T., Lakkala, T., Kozlovsky, A., & Williams, P. J. S. (2002). Electric fields and currents of stable drifting auroral arcs in the evening sector. *Journal of Geophysical Research: Space Physics*, *107*(A12). doi: https://doi.org/10.1029/2001JA009172

Bilitza, D., Altadill, D., Truhlik, V., Shubin, V., Galkin, I., Reinisch, B., & Huang, X. (2017). International reference ionosphere 2016: From ionospheric climate to real-time weather predictions. *Space Weather*, *15*(2), 418-429. doi: https://doi.org/10.1002/2016SW001593

Brekke, A., Hall, C., & Hansen, T. L. (1989). Auroral ionospheric conductances during disturbed conditions. *Annales Geophysicae*, *7*(3), 269-280.

Burnham, K. P., & Anderson, D. R. (2002). *Model Selection and Multimodel Inference* (2nd ed.). Springer. doi: https://doi.org/10.1007/b97636

Cai, L., Aikio, A. T., & Nygrén, T. (2013). Height-dependent energy exchange rates in the high-latitude E region ionosphere. *Journal of Geophysical Research: Space Physics*, *118*, 7369-7383. doi: https://doi.org/10.1002/2013JA019195

Carlson, C. W., Pfaff, R. F., & Watzin, J. G. (1998). The fast auroral snapshot (FAST) mission. *Geophysical Research Letters*, *25*(12), 2013-2016. doi: https://doi.org/10.1029/98GL01592

Cattell, C., Dombeck, J., & Hanson, L. (2013). Solar cycle effects on parallel electric field acceleration of auroral electron beams. *Journal of Geophysical Research: Space Physics*, *118*. doi: https://doi.org/10.1002/jgra.50546

Chapman, S., & Bartels, J. (1940). *Geomagnetism, Vol. II: Analysis of the Data, and Physical Theories.* Oxford Univ. Press, London.

Cortie, S., A. L. (1912). Sun-spots and Terrestrial Magnetic Phenomena, 1898–1911: the Cause of the Annual Variation in Magnetic Disturbances. *Monthly Notices of the Royal Astronomical Society*, *73*(1), 52-60. doi: https://doi.org/10.1093/

mnras/73.1.52

Dahlgren, H., Gustavsson, B., Lanchester, B. S., Ivchenko, N., Brändström, U., Whiter, D. K., ... Marklund, G. (2011). Energy and flux variations across thin auroral arcs. *Annales Geophysicae*, *29*, 1699-1712. doi: https://doi.org/10.5194/angeo-29-1699-2011

Evans, D., & Greer, M. (2004). Polar orbiting environmental satellite space environment monitor - 2 instrument descriptions and archive data documentation. *NOAA Tech. Memo. 1.4*.

Fang, X., Randall, C. E., Lummerzheim, D., Wang, W., Lu, G., Solomon, S. C., & Frahm, R. A. (2010). Parameterization of monoenergetic electron impact ionization. *Geophysical Research Letters*, *37*(22). doi: https://doi.org/10.1029/2010GL045406

Grandin, M., Aikio, A. T., Kozlovsky, A., Ulich, T., & Raita, T. (2017). Cosmic radio noise absorption in the high-latitude ionosphere during solar wind high-speed streams. *Journal of Geophysical Research: Space Physics*, *122*(5). doi: https://doi.org/10.1002/2017JA023923

Hardy, D. A., Gussenhoven, M. S., & Brautigam, D. (1989). A statistical model of auroral ion precipitation. *Journal of Geophysical Research*, *94*, 370. doi: https://doi.org/10.1029/ja094ia01p00370

Hardy, D. A., Gussenhoven, M. S., & Holeman, E. (1985). A statistical model of auroral electron precipitation. *Journal of Geophysical Research: Space Physics*, *90*(A5), 4229-4248. doi: https://doi.org/10.1029/JA090iA05p04229

Hardy, D. A., Gusssenhoven, M. S., Rich, F. J., & Brautigam, D. H. (1991). The average pattern of auroral particle precipitation, its associated conductivity and field aligned currents. *Journal of geomagnetism and geoelectricity*, *43*, 337-351. doi: https://doi.org/10.5636/jgg.43.Supplement1_337

Kaeppler, S. R., Hampton, D. L., Nicolls, M. J., Strømme, A., Solomon, S. C., Hecht, J. H., & Conde, M. G. (2015). An investigation comparing ground-based techniques that quantify auroral electron flux and conductance. *Journal of Geophysical Research: Space Physics*, *120*(10). doi: https://doi.org/10.1002/2015JA021396

Kaeppler, S. R., Sanchez, E., Varney, R. H., Irvin, R. J., Marshall, R. A., Bortnik, J., ... Reyes, P. M. (2020). Chapter 6 - incoherent scatter radar observations of 10–100kev precipitation: review and outlook. In A. N. Jaynes & M. E. Usanova (Eds.), *The dynamic loss of earth's radiation belts* (p. 145-197). Elsevier. doi: https://doi.org/10.1016/B978-0-12-813371-2.00006-8

Kavanagh, A. J., Kosch, M. J., Honary, F., Senior, A., Marple, S. R., Woodfield, E. E., & McCrea, I. W. (2004). The statistical dependence of auroral absorption on geomagnetic and solar wind parameters. *Annales Geophysicae*, *22*(3), 877–887. doi: 10.5194/angeo-22-877-2004

Kirkwood, S. (1988). *SPECTRUM - a Computer Algorithm to Derive the Flux-Energy Spectrum of Precipitating Particles from EISCAT Electron Density Profiles* (Tech. Rep. No. 34). Kiruna, Sweden: Swedish Institute of Space Physics.

Lam, M. M., Horne, R. B., Meredith, N. P., Glauert, S. A., Moffat-Griffin, T., & Green, J. C. (2010). Origin of energetic electron precipitation >30 kev into the atmosphere. *Journal of Geophysical Research: Space Physics*, *115*(A4). doi: https://doi.org/10.1029/2009JA014619

Lehtinen, M. S., & Huuskonen, A. (1996). General incoherent scatter analysis and GUISDAP. *Journal of Atmospheric and Terrestrial Physics*, *58*(1), 435-452. doi: https://doi.org/10.1016/0021-9169(95)00047-X

Liou, K., Newell, P. T., & Meng, C.-I. (2001). Seasonal effects on auroral particle acceleration and precipitation. *Journal of Geophysical Research: Space Physics*, *106*(A4), 5531-5542. doi: https://doi.org/10.1029/1999JA000391

Lockwood, M., Owens, M. J., Barnard, L. A., Haines, C., Scott, C. J., McWilliams,

K. A., & Coxon, J. C. (2020). Semi-annual, annual and universal time variations in the magnetosphere and in geomagnetic activity: 1. geomagnetic data. *Journal Space Weather Space Climate*, *10*, 23. doi: https://doi.org/10.1051/swsc/2020023

Matzka, J., Stolle, C., Yamazaki, Y., Bronkalla, O., & Morschhauser, A. (2021). The Geomagnetic Kp Index and Derived Indices of Geomagnetic Activity. *Space Weather*, *19*(5). doi: https://doi.org/10.1029/2020SW002641

Nanjo, S., Nozawa, S., Yamamoto, M., Kawabata, T., Johnsen, M. G., Tsuda, T. T., & Hosokawa, K. (2022). An automated auroral detection system using deep learning: real-time operation in tromsø, norway. *Scientific Reports*, *12*(1), 8038. doi: https://doi.org/10.1038/s41598-022-11686-8

Newell, P. T., & Gjerloev, J. W. (2011). Evaluation of SuperMAG auroral electrojet indices as indicators of substorms and auroral power. *Journal of Geophysical Research: Space Physics*, *116*(12), 1–12. doi: https://doi.org/10.1029/2011JA016779

Newell, P. T., Liou, K., Sotirelis, T., & Meng, C. I. (2001). Auroral precipitation power during substorms: A Polar UV Imager-based superposed epoch analysis. *Journal of Geophysical Research: Space Physics*, *106*(A12), 28885–28896. doi: https://doi.org/10.1029/2000ja000428

Newell, P. T., Meng, C.-I., & Wing, S. (1998). Relation to solar activity of intense aurorae in sunlight and darkness. *Nature*, *393*(6683), 342-344. doi: https://doi.org/10.1038/30682

Newell, P. T., Sotirelis, T., Liou, K., Meng, C. I., & Rich, F. J. (2007). A nearly universal solar wind-magnetosphere coupling function inferred from 10 magnetospheric state variables. *Journal of Geophysical Research: Space Physics*, *112*(1), 1–16. doi: https://doi.org/10.1029/2006JA012015

Newell, P. T., Sotirelis, T., & Wing, S. (2009). Diffuse, monoenergetic, and broadband aurora: The global precipitation budget. *Journal of Geophysical Research: Space Physics*, *114*(A9). doi: https://doi.org/10.1029/2009JA014326

Newell, P. T., Sotirelis, T., & Wing, S. (2010). Seasonal variations in diffuse, monoenergetic, and broadband aurora. *Journal of Geophysical Research: Space Physics*, *115*(A3). doi: https://doi.org/10.1029/2009JA014805

Newell, P. T., Wing, S., Sotirelis, T., & Meng, C. I. (2005). Ion aurora and its seasonal variations. *Journal of Geophysical Research: Space Physics*, *110*(A1). doi: https://doi.org/10.1029/2004JA010743

Palmroth, M., Grandin, M., Sarris, T., Doornbos, E., Tourgaidis, S., Aikio, A., . . . Yamauchi, M. (2021). Lower-thermosphere–ionosphere (LTI) quantities: current status of measuring techniques and models. *Annales Geophysicae*, *39*(1), 189–237. doi: 10.5194/angeo-39-189-2021

Paschmann, G., Haaland, S., & Treumann, R. (2003). In situ measurements in the auroral plasma. In *Auroral plasma physics* (pp. 93–208). Dordrecht: Springer Netherlands. doi: 10.1007/978-94-007-1086-3_4

Picone, J. M., Hedin, A. E., Drob, D. P., & Aikin, A. C. (2002). NRLMSISE-00 empirical model of the atmosphere: Statistical comparisons and scientific issues. *Journal of Geophysical Research: Space Physics*, *107*(A12), SIA 15-1-SIA 15-16. doi: https://doi.org/10.1029/2002JA009430

Robinson, R. M., Vondrak, R. R., Miller, K., Dabbs, T., & Hardy, D. (1987). On calculating ionospheric conductances from the flux and energy of precipitating electrons. *Journal of Geophysical Research: Space Physics*, *92*(A3), 2565-2569. doi: https://doi.org/10.1029/JA092iA03p02565

Russell, C. T., & McPherron, R. L. (1973). Semiannual variation of geomagnetic activity. *Journal of Geophysical Research (1896-1977)*, *78*(1), 92-108. doi: https://doi.org/10.1029/JA078i001p00092

Semeter, J., & Kamalabadi, F. (2005). Determination of primary electron spectra from incoherent scatter radar measurements of the auroral E region. *Radio*

Science, *40*(2). doi: https://doi.org/10.1029/2004RS003042

Sheehan, C. H., & St-Maurice, J. P. (2004). Dissociative recombination of N2+, O2+, and NO+: Rate coefficients for ground state and vibrationally excited ions. *Journal of Geophysical Research: Space Physics*, *109*(A3), 1–21. doi: https://doi.org/10.1029/2003JA010132

Sigernes, F., Dyrland, M., Brekke, P., Chernouss, S., Lorentzen, D. A., Oksavik, K., & Deehr, C. S. (2011). Two methods to forecast auroral displays. *J. Space Weather Space Clim.*, *1*(1). doi: https://doi.org/10.1051/swsc/2011003

Simon Wedlund, C., Lamy, H., Gustavsson, B., Sergienko, T., & Brändström, U. (2013). Estimating energy spectra of electron precipitation above auroral arcs from ground-based observations with radar and optics. *Journal of Geophysical Research: Space Physics*, *118*(6), 3672-3691. doi: https://doi.org/10.1002/jgra.50347

Starkov, G. V. (1994). Mathematical model of the auroral boundaries. *Geomagnetism and Aeronomy*, *34*(3), 331-336.

Tesfaw, H. W., Virtanen, I. I., Aikio, A. T., Nel, A., Kosch, M., & Ogawa, Y. (2022). Precipitating Electron Energy Spectra and Auroral Power Estimation by Incoherent Scatter Radar With High Temporal Resolution. *Journal of Geophysical Research: Space Physics*, *127*(4). doi: https://doi.org/10.1029/2021JA029880

Thorne, R. M., Bortnik, J., Li, W., & Ma, Q. (2021). Wave–particle interactions in the earth's magnetosphere. In *Magnetospheres in the solar system* (p. 93-108). American Geophysical Union (AGU). doi: https://doi.org/10.1002/9781119815624.ch6

Thorne, R. M., Ni, B., Tao, X., Horne, R. B., & Meredith, N. P. (2010). Scattering by chorus waves as the dominant cause of diffuse auroral precipitation. *Nature*, *467*(7318), 943-946. doi: 10.1038/nature09467

Virtanen, I., & Gustavsson, B. (2018). *ELSPEC*. Zenodo. doi: https://doi.org/10.5281/zenodo.6644454

Virtanen, I., Gustavsson, B., Aikio, A., Kero, A., Asamura, K., & Ogawa, Y. (2018). Electron energy spectrum and auroral power estimation from incoherent scatter radar measurements. *Journal of Geophysical Research: Space Physics*, *123*(8), 6865-6887. doi: https://doi.org/10.1029/2018JA025636

Vondrak, R. R., & Baron, M. J. (1977). A method of obtaining the energy distribution of auroral electrons from incoherent scatter radar measurements. In A. Brekke (Ed.), *Radar probing of the auroral plasma* (p. 315-330). Universitetsforlaget.

Vorobjev, V. G., Yagodkina, O. I., & Katkalov, Y. V. (2013). Auroral Precipitation Model and its applications to ionospheric and magnetospheric studies. *Journal of Atmospheric and Solar-Terrestrial Physics*, *102*, 157–171. doi: https://doi.org/10.1016/j.jastp.2013.05.007

Wissing, J., Bornebusch, J., & Kallenrode, M.-B. (2008). Variation of energetic particle precipitation with local magnetic time. *Advances in Space Research*, *41*(8), 1274-1278. doi: https://doi.org/10.1016/j.asr.2007.05.063

Yakovchuk, O., & Wissing, J. M. (2019). Magnetic local time asymmetries in precipitating electron and proton populations with and without substorm activity. *Annales Geophysicae*, *37*(6), 1063–1077. doi: https://doi.org/10.5194/angeo-37-1063-2019

Yamazaki, Y., Matzka, J., Stolle, C., Kervalishvili, G., Rauberg, J., Bronkalla, O., ... Jackson, D. R. (2022). Geomagnetic activity index Hpo. *Geophysical Research Letters*, *49*(10). doi: https://doi.org/10.1029/2022GL098860

Zhang, Y., & Paxton, L. (2008). An empirical kp-dependent global auroral model based on timed/guvi fuv data. *Journal of Atmospheric and Solar-Terrestrial Physics*, *70*(8), 1231-1242. doi: https://doi.org/10.1016/j.jastp.2008.03.008